Reducing Shimmy Oscillation of Nose Landing Gear Based on a Torsional Nonlinear Energy Sink and an Annular Granular Damper

Tian Nan, Stefano Lenci, Yao Chen, Yu-nan Zhu, Xiang-Ying Guo*

School of Mathematics, Statistics and Mechanics, Beijing University of Technology, Beijing,100124, China

Email: guoxy@bjut.edu.cn

ABSTRACT

Shimmy in nose landing gears may induce high-cycle fatigue in critical structural components and thus poses a safety risk during taxiing, take-off, and landing rollouts. To mitigate shimmy under complex service conditions, this study proposes a passive hybrid suppression concept by integrating a torsional nonlinear energy sink (NES) and an annular granular particle damper (PD) into a single-wheel nose landing gear system. A coupled nonlinear shimmy model involving torsional and lateral bending modes is developed based on the Thota tire force formulation and stretched-string tire deformation dynamics, with geometric effects induced by the rake angle also considered. The torsional NES is realized through a modified roller–spring mechanism, whose nonlinear restoring torque is derived via geometric analysis and cubic Taylor approximation, resulting in near-zero linear stiffness with a positive cubic stiffness component. The annular PD is modeled using a gas–solid two-phase-flow-based equivalent viscous damping approach, and the corresponding torsional damping torque is incorporated into the governing equations. Bifurcation analyses are performed using MATCONT in the (V, Fz)-plane to evaluate the stability boundaries and the oscillation regions of torsional shimmy, lateral bending shimmy, and bistability. The results show that the standalone NES effectively reduces the torsional shimmy region and enlarges the stable domain in the low-load range. In contrast, the standalone PD significantly attenuates vibration amplitudes but enlarges the shimmy region and induces a characteristic “Both” oscillation mode in which torsional and lateral responses coexist. The combined NES–PD configuration simultaneously achieves substantial amplitude reduction and a contraction of the unstable operating region. For a representative low-load case, the maximum torsional amplitude is reduced by about 87% compared with the baseline configuration, while the shimmy speed interval is also decreased. A parametric study is further conducted to evaluate the influence of key NES and PD parameters, including the concave track radius, spring pre-stretch, spring stiffness, roller radius, particle filling ratio, and particle density, on the shimmy suppression performance.

KEYWORDS: Aircraft dynamics; Bifurcation analysis; Shimmy oscillations; Nonlinear energy sink(NES).

1. Introduction

Landing gear is a critical subsystem of an aircraft, providing essential functions during takeoff and landing such as alleviating touchdown impacts, enabling braking, and maintaining directional control, and it therefore serves as a primary means of ground-motion control for the aircraft [1]. Maintaining adequate landing-gear stability is thus of great importance [2]. During ground roll, external disturbances may induce a certain wheel yaw angle, and if periodic or divergent oscillations persist after the disturbance vanishes, the landing gear is considered to have insufficient stability; this phenomenon is commonly referred to as shimmy in aeronautic engineering. Shimmy may occur in both nose and main landing gears [3-5], but it is more frequently observed in the nose landing gear. It is typically a self-excited vibration dominated by the coupled torsional and lateral bending modes [6]. Such oscillations are detrimental to aircraft ground operations and may lead to component damage, injuries to crew and passengers, and even serious accidents. For this reason, shimmy mitigation and suppression should be addressed during the aircraft design stage.

As a complex mechanical system, a landing gear involves multiple degrees of freedom and various nonlinear effects, and dynamic modeling therefore requires a balance between accuracy, reliability, and an appropriate selection of dominant physical factors. Somieski developed a shimmy model based on the torsional mechanics of a nose landing gear and a stretched-string tire representation, and investigated wheel shimmy using both linearized and nonlinear approaches. Numerical simulations under large-amplitude conditions showed that the linear and nonlinear predictions agree in stable regimes, while in unstable regimes the nonlinear response is bounded by a stable outer limit cycle [7]. Rahmani et al. established a nonlinear nose landing gear model in the MATLAB Simscape Multibody environment, incorporating torsional, lateral, yaw, and axial degrees of freedom as well as Coulomb friction nonlinearity, and they quantified the influence of friction parameters on stability. In addition, a torque-link mechanism was included and topology optimization was performed on the torque link to improve the fidelity of shimmy prediction [8-11]. Feng and Jiang constructed nonlinear landing-gear models in the LMS platform to examine the effect of structural clearances on shimmy [12,13]. Du et al. further considered torsional freeplay in a dual-wheel nose landing gear under stochastic crosswind disturbances and found that, compared with the no-clearance case, freeplay enlarges the shimmy region and intensifies the oscillation characteristics [14]. Gao et al. proposed a six-degree-of-freedom mathematical model for a dual-wheel nose landing gear that includes strut longitudinal bending and axial displacement, and treated torque-link clearance as an explicit term; their numerical results indicated that clearances on both sides of the lower torque-link joint lead to a wider torsional shimmy range than a unilateral clearance case [15]. Thota et al. developed a seven-degree-of-freedom model incorporating torsional, lateral, and longitudinal motions, capturing the coupled torsional and lateral bending modes of the landing gear and elastic tire as well as geometric effects introduced by the rake angle. Bifurcation analysis revealed that torsional shimmy, lateral shimmy, and transient quasi-periodic oscillations can all be triggered, while the longitudinal degree of freedom does not play an active role in any of the possible shimmy types. They also established a five-degree-of-freedom model accounting for tire deformation and ground roll dynamics, considered the rake-angle-induced variation of the effective caster length, and investigated the relationship between shimmy characteristics and tire inflation pressure. The results showed that both torsional and lateral shimmy become less likely when the inflation pressure exceeds the nominal value, and increasing the inflation pressure reduces the tendency of the system to jump into high-amplitude shimmy responses [6,16-18]. Jiang et al. incorporated an oleo-pneumatic shock absorber structure into the conventional landing gear model, through which time-varying loads associated with different stroke conditions were introduced. The influence of these time-varying loads on shimmy performance was subsequently investigated [19]. Ruan et al., based on an experimentally derived tire contact trajectory hypothesis, examined the effects of tire profile geometry and contact surface conditions on the shimmy stability of landing gear [20]. Wu et al. focused on the nose landing gear of an unmanned aerial vehicle and proposed a multibody dynamic simulation approach for reproducing shimmy behavior. The method accounts for multiple factors, including air spring force, hydraulic damping force, tire forces, and structural stiffness, and yields shimmy damping values capable of satisfying stability requirements for the nose landing gear [21].

An accurate shimmy model is essential for reliably characterizing the nonlinear dynamic behavior of landing gears, while properly designed suppression devices can effectively attenuate shimmy responses. In general, shimmy mitigation strategies can be classified into two main categories. The first relies on introducing strong nonlinear stiffness through structural design to reduce both the instability region and vibration amplitude, with the nonlinear energy sink (NES) being a representative approach [22,23]. Sanches et al. investigated an NES implemented by attaching an ideal cubic nonlinear spring at the wheel axle in a landing gear system, and numerical results demonstrated that an appropriate nonlinear stiffness configuration can significantly decrease the shimmy occurrence range [24]. Guo et al. further performed a reliability assessment of NES-based absorbers, confirming the feasibility and robustness of nonlinear stiffness absorbers for aircraft safety-oriented design [25]. Wang et al. proposed a torsional NES design for a dual-wheel nose landing gear, which effectively reduced the torsional shimmy region and, in certain cases, markedly decreased the vibration amplitude [26,27]. Friskney et al. explored the suppression of torsional vibration in gear-like transmission structures through nonlinear coupling elements, and such concepts can also provide useful references for torsional shimmy mitigation [28]. Besides, several studies have explored the application of NES in other nonlinear self-excited vibration systems, including fluid-conveying systems [29-32], Van der Pol (VDP) oscillators [33], rotor systems [34], and aeroelastic wings [35]. However, the mechanisms and effectiveness of NES in suppressing the dynamic responses of such systems remain not yet fully understood. In particular, increasing linear damping may induce structural instability in self-excited systems, a phenomenon commonly referred to as the “flutter paradox” [36,37]. The second category focuses on damping-oriented control by introducing nonlinear damping terms into the landing gear structure, aiming to improve suppression performance during shimmy while limiting the impact on the baseline damping characteristics and normal operational behavior. Dong et al. studied the use of magnetorheological dampers for shimmy suppression in landing gear systems [38]. Wang et al. proposed a nonlinear feedback control strategy based on the linear term of the torsional angle to regulate and suppress shimmy, which can be regarded as a form of nonlinear damping implementation [39]. Tartaruga et al. applied two novel optimization-based control approaches to landing gear shimmy and achieved effective vibration reduction [40]. Among various nonlinear damping devices, particle dampers have attracted increasing attention due to their simple configuration and strong inherent nonlinearity [41,42]. Therefore, exploring particle dampers as nonlinear damping components for shimmy suppression is both meaningful and necessary.

Current studies on nonlinear shimmy models predominantly employ numerical continuation techniques. The main advantage of this approach lies in its ability to systematically track equilibrium solutions and periodic responses as system parameters vary, and it remains effective even when asymptotic stability conditions are not strictly satisfied. In practical engineering applications, numerical continuation is typically implemented through dedicated software packages, among which AUTO [43] and MATCONT [44] are widely used.

In this work, a torsional nonlinear energy sink based on nonlinear stiffness design and an annular particle damper acting as a nonlinear damping device are first introduced, followed by the formulation of the coupled shimmy governing equations and the incorporation of the proposed suppression components. To the best of authors' knowledge, this vibration reduction system has not been investigated before, and it is promising in terms of expected performance.

Nonlinear energy sinks (NES) have been demonstrated to be effective in reducing both the shimmy region and the vibration amplitude by introducing strong nonlinear stiffness into the system [24-28]. However, in practical applications, the extent of amplitude reduction achieved by NES alone is often limited. In contrast, damping-based devices such as particle dampers can significantly attenuate vibration amplitudes due to their strong energy dissipation capability, while their influence on the extent of the instability region remains less well understood.

Considering the complementary characteristics of these two approaches, combining a nonlinear stiffness based NES with a nonlinear damping device such as a particle damper provides a promising strategy for improving shimmy suppression performance. The NES primarily contributes to reducing the instability region and enhancing overall stability, while the particle damper enhances energy dissipation and suppresses vibration amplitudes. Therefore, in this study, a coupled NES-PD suppression configuration is introduced and incorporated into the nose landing gear shimmy model, and its dynamical behavior and suppression performance are systematically investigated.

The shimmy suppression performance is evaluated for three configurations, namely the NES-only case, the PD-only case, and the combined NES-PD case, through bifurcation analysis in the (forward velocity, vertical landing gear force) parameter plane as well as time-domain simulations at representative operating points. In this study, the suppression performance is assessed in terms of two aspects: the ability to avoid the onset of shimmy by enlarging the stable region in the parameter plane, and the capability to reduce vibration amplitudes when shimmy occurs. Finally, the influence of key design parameters of both the torsional NES and the particle damper on the overall suppression performance is systematically investigated.

2. Mathematical model

2.1. Dynamics of the torsional NES

The torsional NES concept is derived from a modified slider-roller mechanism originally associated with a three-spring negative-stiffness configuration. Two symmetric spring-roller-slider assemblies acting in the vertical direction are installed in an opposing arrangement inside the shock strut, between the inner and outer cylinders. The overall configuration is illustrated in Figure 1a, and the detailed top view is provided in Figure 1b. To prevent the roller from leaving the track during torsional motion, the roller is embedded within the guide rail, and the spring force is oriented from the inner cylinder toward the outer cylinder. In each of the four directions, one end of the spring is attached to the outer cylinder and the other end is connected to the roller. The roller is located inside the inner cylinder and moves along the circumferential path of the outer surface of the inner cylinder when torsion occurs. The outer cylinder is connected to the upper landing-gear structure, while the inner cylinder is connected to the lower part of the landing gear.

The spring stiffness is denoted by k_s, the inner-cylinder radius by r_1, the radius of the concave track by r_2, and the roller radius by r_3. The embedded cylindrical element has an insertion angle of $\pi/3$. The contact friction between the roller and the outer surface of the inner cylinder is neglected due to the smooth surfaces of both components. Under these assumptions, the proposed torsional NES provides an effective nonlinear stiffness contribution to the landing gear system. The specific parameters of NES are shown in Table 1.

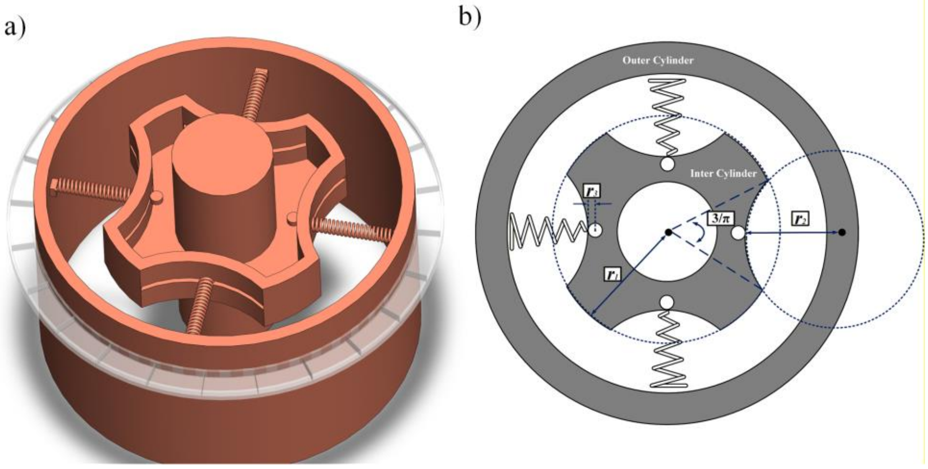

Figure 1. Schematic of the torsional NES integrated into the nose landing gear.
a) Overall configuration; b) Detailed top view.

Table 1. NES parameters and their values in the modelling

Simbel	parameter	Value	Unit
r_1	Radius of strut inner-cylinder	0.1	m
r_2	Radius of the concave track	0.07-0.09	m
r_3	Radius of roller	0.02-0.005	m
k_s	Spring stiffness	1.0-1.4 10^6	N m
e_p	Spring pre-stretch	0.5-0.05	mm

Next, a static analysis is carried out for the torsional NES to characterize the relationships between the torsional angle and the generated restoring torque, as well as the variation of the equivalent stiffness with respect to the torsional deformation. Figure 2 illustrates the NES configuration at the initial state and under torsional deflection. In the initial configuration shown in the left panel of Figure 2, the strut center, the roller center, and the center of the concave cylindrical track are aligned on the same straight line. The roller is located at the midpoint of the arc-shaped trajectory, and the spring force acting at the roller-inner cylinder contact is directed outward. Under this condition, the moments produced by the contact forces remain in equilibrium. When the NES undergoes torsional motion, a torsional deformation and a corresponding torsional angle are introduced, resulting in a restoring moment generated by the mechanism. The deflected configuration is shown in the right panel of Figure 2. The distance between the strut center and the orthogonal force center is denoted by d, and the spring pre-stretch deformation is represented by e_p. Based on the geometric characteristics of the NES, the spring force F and the lever arm d can be expressed as follows:

$$F = k_s\left(e_p - \left(r_1 - r_3 - \left(1 - \sqrt{3}/2\right)(r_1 + r_2)\right) + \Delta\right)(r_2 + r_3)/\tau, \tag{1}$$

$$d = \Delta Sin(\psi^*)\, a/(r_2 + r_3), \tag{2}$$

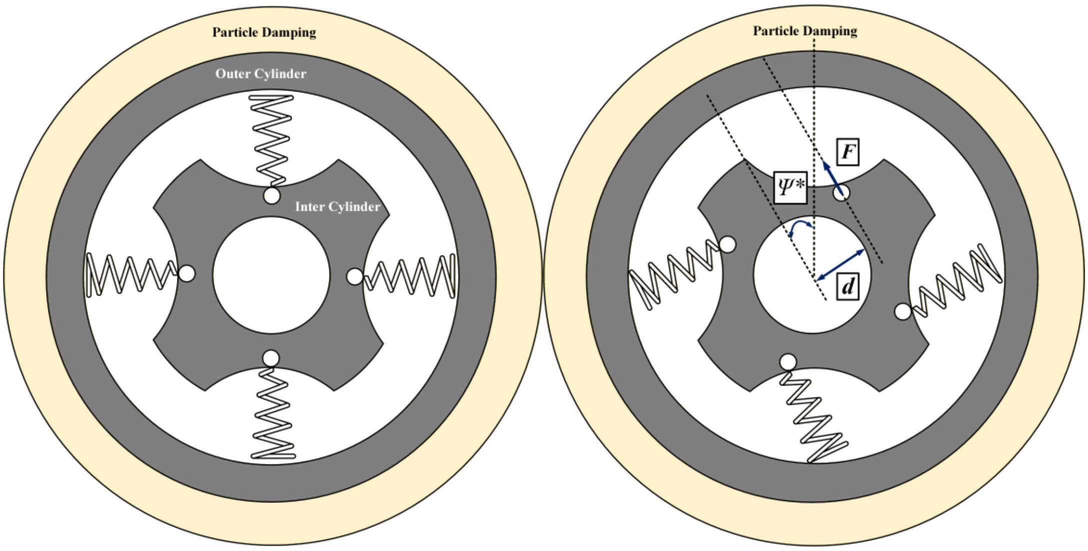

Figure 2. Geometry of the torsional NES at the initial and deflected states

where the intermediate geometric quantities a, τ, and Δ are defined as follows

$$a = \left(\sqrt{3}/2\right)(r_1 + r_2), \tag{3}$$

$$\tau = \sqrt{(r_2 + r_3)^2 - (Sin(\psi^*)a)^2}, \tag{4}$$

$$\Delta = Cos(\psi^*)a - \tau. \tag{5}$$

Accordingly, the restoring torque of the torsional NES can be written as

$$M = 4Fd. \tag{6}$$

The equivalent torsional stiffness of the NES is obtained by differentiating the restoring torque with respect to the torsional angle, namely,

$$k_{nes} = d(M)/d(\psi^*). \tag{7}$$

It can be observed that when the torsional angle is zero, both the NES restoring torque and the corresponding stiffness vanish, this latter is absence of pre-stretch. As the torsional angle increases, the roller may approach the geometric limit of the concave track and then leave the current track segment to enter another arc, with the critical angle given by $6/\pi$. However, experimental observations indicate that the torsional shimmy amplitude is far smaller than this critical value. Therefore, for torsional angles below the critical threshold, the roller remains in proper contact with the concave track and the mechanism operates in its intended working condition.

Assuming that the torsional angle is sufficiently small, the restoring torque can be approximated by a third-order Taylor expansion as

$$M \cong k_1\psi^* + k_3(\psi^*)^3. \tag{8}$$

As shown in Figure 3, the exact nonlinear expressions of the restoring torque and the equivalent stiffness are well approximated by the third-order Taylor series in the low-angle range, and the discrepancy between the two descriptions remains small. In addition, the linear stiffness term is positively correlated with the spring pre-stretch and becomes zero when no pre-stretch is applied; when the pre-stretch is small, the linear term can be neglected. As a result, the proposed torsional NES can be regarded as an NES with near-zero linear stiffness and a positive cubic stiffness component.

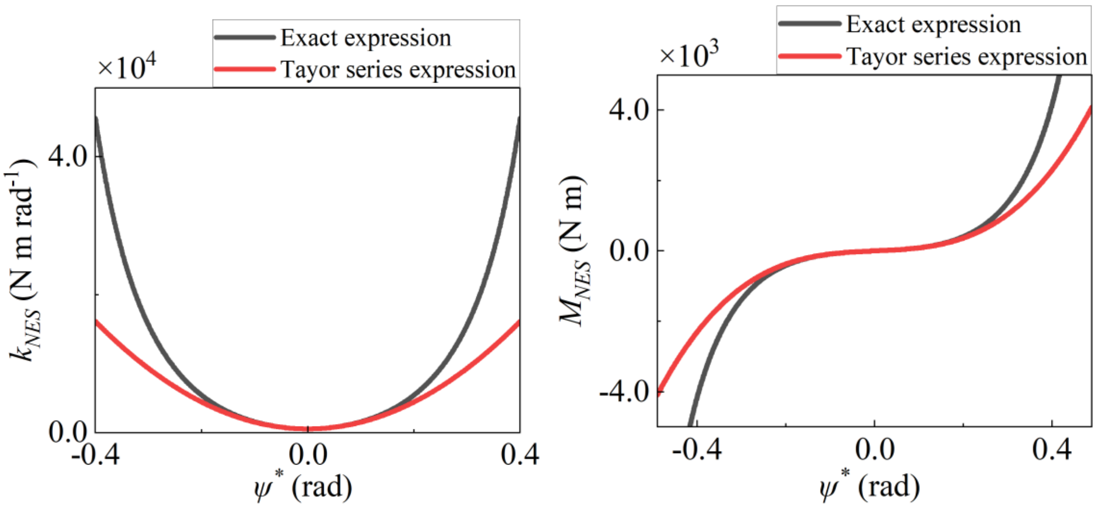

Figure 3. Exact nonlinear restoring torque and equivalent stiffness versus their third-order Taylor approximations

2.2. Dynamics of the annular granular particle damper

The annular particle damper is arranged as a square-section ring wrapped around the outer cylinder of the shock strut, as shown in Figure 4. The particle damping ring has a height $H = 0.1$m, an inner diameter $d_i = 0.24$m, an outer diameter $d_o = 0.36$m, a width of 0.06 m, and a centerline radius $r = 0.15$m. The ring damper is divided into n square-section damping segments and can be approximated as a continuous assembly of individual particle damper units connected along the circumferential direction, while its cross-sectional area can be approximated by the base area of a single unit damper.

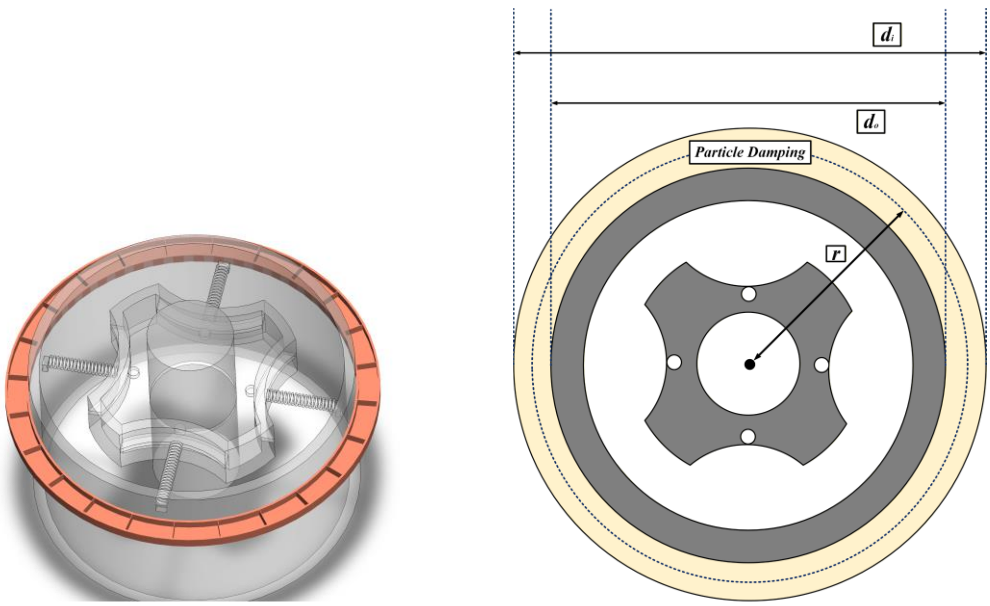

Figure 4. Schematic of the annular particle damper integrated into the nose landing gear.

To establish the dynamic response model of the annular particle damper, the gas-solid two-phase flow theory for particle damping systems is adopted [42]. This model has been widely used, and the damping effect is attributed to contact dissipation caused by particle collisions and friction, together with non-contact dissipation associated with kinetic energy transfer. Following this principle, the dissipation contributions from both the gas and solid phases are represented in terms of an equivalent viscous damping. The classical formulation is usually derived for a single-degree-of-freedom container with the particle translational velocity $\dot{x}$ as the state variable. For the present particle damping ring, which is approximated as a continuous connection of multiple unit cells, the torsional angle ψ is adopted as the corresponding state variable, so that

$$\dot{x} = r\dot{\psi}. \tag{9}$$

The corresponding tangential damping force is given by:

$$F_{pd} = c_{eq}^{*}(\dot{x})\dot{x}. \tag{10}$$

The associated damping moment arm with respect to the rotation axis is given by:

$$M_{pd} = rF_{pd} = rc_{eq}^{*}\left(r|\dot{\psi}|\right)\left(r\dot{\psi}\right) = r^2 c_{eq}^{*}\left(r|\dot{\psi}|\right)\dot{\psi}. \tag{11}$$

Accordingly, the equivalent damping coefficient is expressed as:

$$c_{eq} = nr^2 c_{eq}^{*}\left(r|\dot{\psi}|\right) \tag{12}$$

Following the equivalent viscous particle damping model based on the gas-solid two-phase flow theory (PGS) we have

$$c_{eq}^{*}\left(r|\dot{\psi}|\right) = c_c + c_f + c_k, \tag{13}$$

where:

Collision term c_c:

$$c_c = c_{11}(r|\dot{\psi}|)^{\frac{1}{2}} + c_{21}r|\dot{\psi}| - c_{31}\left(r|\dot{\psi}|\right)^{\frac{3}{2}} \tag{14}$$

$$c_{11} = 4\bar{c}\alpha^{\frac{1}{2}}f^{\frac{1}{2}} \quad c_{21} = 4\bar{c} \quad c_{31} = 4\bar{c}\alpha^{\frac{3}{2}}f^{-\frac{1}{2}} \tag{15}$$

$$\alpha = \frac{1}{5}\sqrt{\frac{6}{\pi}\frac{(1-e_r){\alpha_p}^2 g_p\rho_p d_p}{\pi d^2\rho_m}} \tag{16}$$

$$\bar{c} = \frac{9}{16}\pi^3 d^2 h\rho_m \tag{17}$$

Friction term c_f:

$$c_f = c_{12} r|\dot{\psi}| + c_{22}\left(r|\dot{\psi}|\right)^2 + c_{32}\left(r|\dot{\psi}|\right)^3 \tag{18}$$

$$c_{12} = 4\bar{c}\alpha_1^{\frac{1}{2}} f^{-\frac{1}{2}} \quad c_{22} = 4\bar{c}\alpha_1 \quad c_{32} = 4\bar{c}\alpha_1^{\frac{3}{2}} f^{-\frac{1}{2}} \tag{19}$$

$$\alpha_1 = \frac{\left[\alpha_p\rho_p + \rho_p(1+e_r)\alpha_p{}^2 g_p\right]\sin\phi}{12\pi d^2\rho_m\sqrt{I_{2D}}} \tag{20}$$

Kinetic (non-contact) term c_k:

$$c_k = c_{13}(r|\dot{\psi}|)^{\frac{1}{2}} + c_{23} r|\dot{\psi}| - c_{33}\left(r|\dot{\psi}|\right)^{\frac{3}{2}} \tag{21}$$

$$c_{13} = \frac{3\rho_m h d^2\pi^3}{4}\alpha_3^{\frac{1}{2}} f^{\frac{1}{2}} \quad c_{23} = \frac{3\rho_m h d^2\pi^3}{4}\alpha_3 \quad c_{33} = \frac{3\rho_m h d^2\pi^3}{16}\alpha_3^{\frac{3}{2}} f^{-\frac{1}{2}} \tag{22}$$

$$\alpha_3 = \frac{\sqrt{6\pi}\rho_p d_p\left[25 + 40\alpha_p g_p(1+e_r) + 64\alpha_p{}^2 g_p{}^2(1+e_r)^2\right]}{1440\pi d^2\rho_m\alpha_p g_p(1+e_r)} \tag{23}$$

Here, a_p denotes the mass filling ratio, typically ranging from 0.50 to 0.95; ρ_p is the particle density, with typical values of about 7800 kg/m^3 for steel shot and 16,000-17,000 kg/m^3 for tungsten powder; ρ_m is the mixture density and is commonly taken as $(0.8\text{-}0.95)\rho_p$ based on the particle volume fraction; g_p is the radial distribution function, usually in the range 1.2-5.0 for dense granular beds and approximately 1 for loose beds; e_r is the coefficient of restitution, typically 0.5-0.9, with representative values of about 0.6 for tungsten and 0.8 for steel; d and h represent the chamber diameter and chamber height, respectively; d_p is the mean particle diameter, generally 0.3-2.0 mm and often taken as about 1 mm in practice. The correction factor f is a dimensionless amplification coefficient that accounts for dense packing effects and the influence of the radial distribution in the PGS model. For typical dense filling ratios in the range 0.80-0.95, f commonly falls between about 10 - 30. In addition, ϕ is the internal friction angle, typically $25° - 40°$ and about $35°$ for steel shot, and I_{2D} is the second invariant of the deviatoric stress tensor, which is usually taken as approximately 1 under fully sheared conditions. The specific parameters of PD are shown in Table 2.

Table 2. PD parameters and their values in the modelling

Simbel	parameter	Value	Unit
H	Height of particle damping ring	0.1	m
d_i	Diameter of inter PD ring	0.24	m
d_o	Diameter of outer PD ring	0.36	m
n	Number of damping segments	24	-
a_p	Mass filling ratio	0.5-0.95	-
ρ_p	Particle density	7800-17000	kg m^3
g_p	Radial distribution function	1.0-5.0	-
e_r	Coefficient of restitution	0.5-0.9	-
d_p	Diameter of mean particle diameter	0.5-2.0	mm
f	Correction factor	10-30	-

ϕ	Internal friction angle	0.3491-0.6981	rad
I_{2D}	Second invariant of the deviatoric stress tensor	1	-

The resulting equivalent viscous damping c_{eq} of the annular particle damper obtained from the above formulation is illustrated in Figure 5.

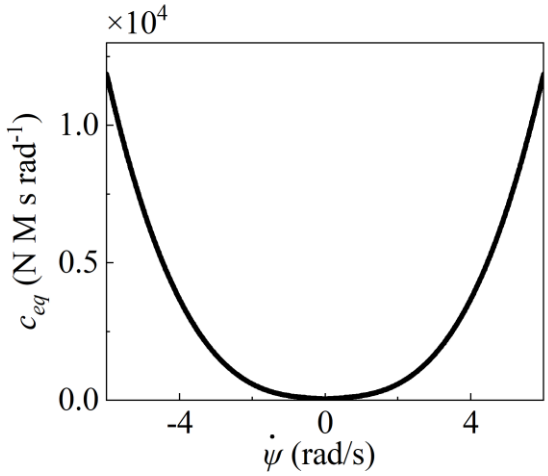

Figure 5. Equivalent viscous damping of the annular particle damper.

2.3. Shimmy dynamic model with the torsional NES and annular granular particle damper

A single-wheel nose landing gear model subjected to a vertical load F_z is established. The installation point of the landing gear is located at a height L_g above the ground, and the landing gear moves together with the aircraft at a constant forward speed V, while a wheel of radius R rolls straight along the runway. As shown in Figure 6, a standard coordinate system is adopted, where the x-axis points rearward along the aircraft longitudinal direction, the z-axis is vertically upward normal to the ground, and the y-axis points inward according to the right-hand rule. The landing gear strut can rotate about the steering axis S with a torsional angle ψ. In addition, the strut undergoes lateral bending deformation δ about the x-axis. The strut is connected to the wheel axle through a caster length e. The strut is inclined from the vertical direction by a rake angle φ. Owing to the nonzero rake angle, the wheel steering angle satisfies the relationship

$$\theta = \psi \cos\varphi. \tag{24}$$

In Eq. (24), θ denotes the wheel steering angle. Meanwhile, to account for the influence of the rake angle on the caster length, a geometric expression for the effective caster length is introduced:

$$e_{eff} = e \cos\varphi + (R + e \sin\varphi) \tan\varphi, \tag{25}$$

where e_{eff} is the effective caster length, φ is the landing-gear rake angle, and R is the wheel radius.

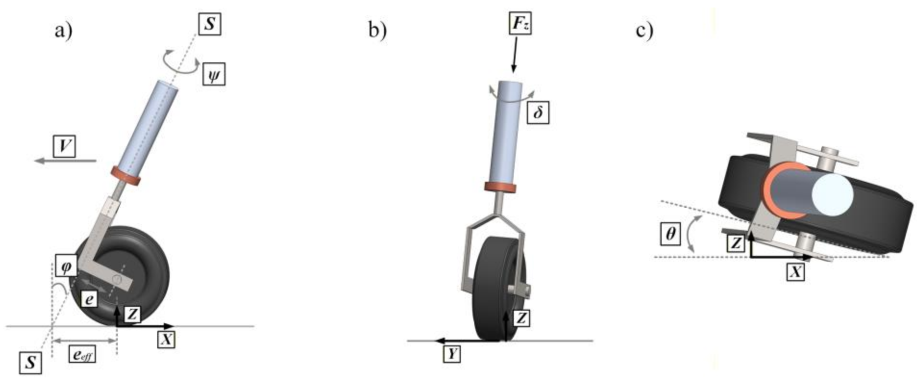

Figure 6. Schematic diagram of nose landing gear a) side view; b) front view; c) top.

By considering the torsional motion of the nose landing gear, the lateral bending deformation of the strut, and the lateral displacement of the wheel, a set of coupled shimmy governing equations is formulated using the empirical tire model proposed by Thota:

$$I_z\ddot{\psi}+c_\psi\dot{\psi}+k_\psi\psi+M_{k_a}+e_{eff}F_{k_\lambda}+M_{D_\lambda}-F_z\,sin(\varphi)\,e_{eff}\,sin(\theta)=0, \tag{26}$$

$$I_x\ddot{\delta}+c_\delta\dot{\delta}+k_\delta\delta+(l_g)F_{k_\lambda}\,cos(\theta)\,cos(\varphi)-F_z e_{eff}\,sin(\theta)=0, \tag{27}$$

$$\dot{\lambda}+\frac{V}{L}\lambda-V\,sin(\theta)-(l_g)\dot{\delta}\,cos(\delta)-(e_{eff}-h)\,cos(\theta)\,\dot{\psi}\,cos(\varphi)=0. \tag{28}$$

In Eq. (26), $M_{K_\psi}=k_\psi\psi$ and $M_{D_\psi}=c_\psi\dot{\psi}$ represent the stiffness and damping-induced torque terms associated with the torsional mode under the torsional inertia moment I_ψ. Correspondingly, in Eq. (27), $M_{K_\delta}=k_\delta\delta$ and $M_{D_\delta}=c_\delta\dot{\delta}$ denote the stiffness and damping-induced moment terms of the lateral bending mode associated with the bending inertia moment I_δ. As can be seen from Eq. (24), Eqs. (26) - (28) include not only the nonlinear forces arising from the tire-ground interaction, but also geometric nonlinear terms.

By distributing the vertical load applied to the tire, the lateral force of each tire can be expressed as

$$F_{K_\lambda}=k_\lambda\tan^{-1}(7\tan(\alpha^*))\cos(0.95\tan^{-1}(7\tan(\alpha^*)))\,F_z. \tag{29}$$

In Eq. (29), k_λ denotes the lateral stiffness of the tire, and the slip angle α^* is related to the lateral tire deformation λ through the following relationship

$$\alpha^*=tan^{-1}\left(\frac{\lambda}{L}\right). \tag{30}$$

In Eq. (30), L is the tire relaxation length. For aircraft tires, the non-uniform contact patch generally leads to distinct sliding and adhesion regions during lateral displacement, which gives rise to a self-aligning moment about the strut steering axis S.

This self-aligning moment is a nonlinear function of the vertical load F_z and can be approximated as

$$M_{k_\alpha}=\begin{cases} k_a\dfrac{\alpha_m}{\pi}sin\left(\dfrac{\alpha^*\pi}{\alpha_m}\right)F_z & \text{if } |\alpha^*|\le\alpha_m, \\ 0 & \text{if } |\alpha^*|>\alpha_m, \end{cases} \tag{31}$$

where k_a is the self-aligning moment stiffness coefficient.

In addition, due to the lateral damping effect of the tire, the tire width may influence the stability of the nose landing gear, and the corresponding tire damping moment is

$$M_{D_\lambda} = \frac{c_\lambda \dot{\psi} \cos(\varphi)}{V}, \tag{32}$$

where c_λ is the lateral damping coefficient of the tire.

The torsional and lateral bending shimmy modes are coupled through the deformation of the tire at the contact patch. In Eq. (26), the torque contribution associated with the tire lateral force, $F_{K_\lambda} e_{eff}$, depends on both the torsional variable ψ and the lateral bending variable δ. Similarly, the self-aligning moment term M_{K_α} is also governed by the combined effects of ψ and δ. Meanwhile, in Eq. (27), the tire-force-related moment term M_{λ_δ} is likewise coupled with ψ and δ. Their explicit expressions are given as follows:

$$M_{\lambda_\delta} = l_g F_{K_\lambda} \cos\theta \cos\varphi. \tag{33}$$

In these expressions, l_g denotes the distance from the landing-gear attachment point on the airframe to the ground. The terms introduced above jointly lead to the coupling between the two shimmy vibration modes in the nose landing gear model.

Eq. (28) describes the tire dynamics of the wheel, and it is formulated based on the stretched-string tire model.

The conventional stretched-string representation is given by:

$$\dot{\lambda} + \frac{V}{L}\lambda = V \sin(\theta) + (e - h)\cos(\theta)\,\dot{\theta}. \tag{34}$$

Eq. (34) is established by considering the relationship between the tire torsional motion and the lateral tire deformation. Since the present nose landing gear model also includes lateral bending of the strut, the kinematic relationship between the tire deformation and the lateral bending variable is further introduced:

$$\dot{\lambda} + \frac{V}{L}\lambda = (l_g)\dot{\delta}\cos(\delta). \tag{35}$$

By combining Eqs. (40) and (41), the tire deformation Eq. (34) is obtained, in which the coupling between the torsional motion and the lateral bending deformation is explicitly included.

The term M_{NES} represents the restoring torque generated by the torsional NES, including a damping contribution, a linear stiffness component, and a cubic stiffness component:

$$M_{NES} = c_{nes}(\dot{\psi} - \dot{\psi}^*) + k_1(\psi - \psi^*) + k_3(\psi - \psi^*)^3. \tag{36}$$

Meanwhile, the nonlinear torsional equation governing the NES internal motion is

$$I_{nes}\ddot{\psi}^* + c_{nes}(\dot{\psi}^* - \dot{\psi}) + k_1(\psi^* - \psi) + k_3(\psi^* - \psi)^3. \tag{37}$$

For the equivalent damping contribution of the particle damper, M_{pd} denotes the particle-damping torque, and the rotational inertia of the particles and the enclosure is represented by the term $I_{\text{pd}}\ddot{\psi}$.

Accordingly, the coupled shimmy governing equations incorporating both the NES and PD can be expressed as follow:

$$I_z\ddot{\psi} + I_{\text{pd}}\ddot{\psi} + c_\psi\dot{\psi} + k_\psi\psi + M_{k_\alpha} + e_{eff}F_{k_\lambda} + M_{D_\lambda} + M_{\text{NES}} + M_{\text{pd}} - F_z \sin(\varphi)\, e_{eff} \sin(\theta) = 0, \tag{38}$$

$$I_x\ddot{\delta} + c_\delta\dot{\delta} + k_\delta\delta + (l_g)F_{k_\lambda}\cos(\theta)\cos(\varphi) - F_z e_{eff}\sin(\theta) = 0, \tag{39}$$

$$\dot{\lambda} + \frac{V}{L}\lambda - V\sin(\theta) - (l_g)\dot{\delta}\cos(\delta) - (e_{eff} - h)\cos(\theta)\,\dot{\psi}\cos(\varphi) = 0. \tag{40}$$

3. Shimmy analysis

In this section, bifurcation analysis is performed using the numerical continuation software MATCONT.

3.1. Comparison of Shimmy Stability Regions in the (V, F_z)-Plane

When the wheel rolls straight ahead, the desired equilibrium state of the system corresponds to a trivial equilibrium in which all state variables remain at zero, namely, the landing-gear strut exhibits no torsional rotation or lateral bending deformation, and the tire contact point has no lateral displacements. Accordingly, shimmy bifurcation analysis is typically focused on the stability of this zero equilibrium and on the associated Hopf bifurcations and periodic solutions that emanate from it.

Table 3. The main landing gear parameters and their values in the modelling

Simbel	parameter	Value	Unit
I_z	Moment of inertia of strut w.r.t. Z-axis	100	kg m2
R	Radius of nose wheel	0.362	m
φ	Rake angle	0.1571(9°)	rad
k_ψ	Torsional stiffness of strut	3.8e5	N m rad-1
c_ψ	Torsional damping of strut	300	N m s rad-1
k_a	Self-aligning coefficient of elastic tire	1.0	m rad-1
α_m	Self-aligning moment limit	0.1745(10°)	rad
c_λ	Damping coefficient of elastic tire	570	N m2 rad-1
k_δ	Lateral bending stiffness of strut	6.1e6	N m rad-1
c_δ	Lateral bending damping of strut	300	N m s rad-1
l_g	Gear height	2.5	m
I_x	Moment of inertia of strut w.r.t. X-axis	600	kg m2
h	Contact patch length	0.1	m
L	Relaxation length	0.3	m
e	Wheel caster length	0.12	m
V	Forward velocity	1-500	m s-1
F_z	Vertical landing gear force	10-500	kN

In shimmy bifurcation studies, the forward velocity of the aircraft nose landing gear and the vertical load acting on the wheel are commonly selected as the two control parameters. In the resulting (V, F_z)-plane, the dominant torsional shimmy region, the lateral bending shimmy region, and the bistable region where both oscillation modes coexist are separated by distinct stability boundaries. This parameter plane provides an intuitive representation of the shimmy stability characteristics of the nose landing gear. Consequently, in studies on shimmy control, the (V, F_z)-plane is widely adopted as a quantitative measure to evaluate the effectiveness of different suppression strategies, and thus it is also employed in the present work to assess the shimmy stability performance.

The (V, F_z)-planes are constructed for four cases, namely the original configuration, the configuration with a torsional NES, with a particle damper (PD), and with both PD and NES, respectively. The main landing gear parameters are listed in Table 3, while the parameters of the NES and the particle damper are given in Tables 1 and 2, respectively.

Figure 7a compares the shimmy behavior of the configuration equipped with the NES with that of the original configuration. In this figure, the shaded regions correspond to the stability map of the configuration with the NES. The region with left-diagonal hatching denotes the lateral bending shimmy domain, the region with right-diagonal hatching corresponds to the torsional shimmy domain, and the cross-hatched region represents the bistable vibration domain where both shimmy modes coexist. The blank area indicates the stable region of the NES-equipped configuration. The blue solid curves denote the Hopf bifurcation boundaries of the configuration with the NES, on which degenerate Hopf (DH) points are identified. The region above the DH point corresponds to the subcritical Hopf regime. From each DH point, a saddle-node bifurcation of periodic orbits emerges, which is indicated by blue dash-dotted curves. The short-dashed curves represent the torus bifurcation boundaries of the NES configuration. For comparison, the black curves depict the bifurcation structure of the original configuration without the NES. The black solid and short-dashed curves correspond to the Hopf and torus bifurcation boundaries, respectively, while the black dash-dotted curves represent the saddle-node bifurcation of periodic orbits originating from the DH points of the original system.

The results clearly show that the introduction of the NES reduces the torsional shimmy region and enlarges the stable domain in the low vertical-load range compared with the original configuration. In addition, at higher forward speeds, both the torsional Hopf boundary and the saddle-node bifurcation curves emanating from the DH points contract markedly, leading to the transformation of part of the bistable region of the original configuration into a lateral bending shimmy region. Notably, the minimum vertical load required for the onset of shimmy is increased by 22.6% when the NES is installed. Moreover, the pure torsional shimmy region in the low vertical-load range is reduced by approximately 35%. These results demonstrate that the NES is effective in suppressing the shimmy region, particularly by expanding the stable operating range under practically relevant low vertical-load conditions.

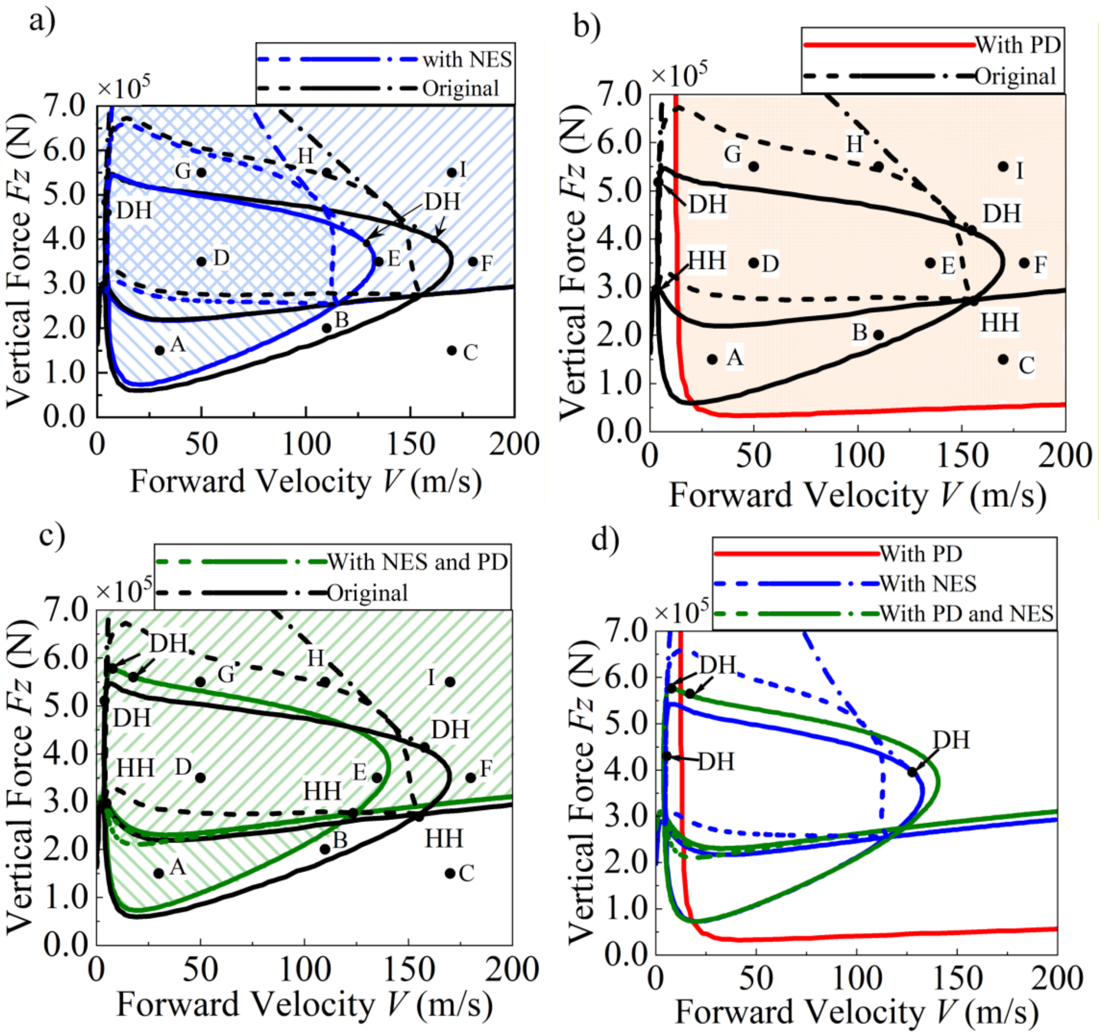

Figure 7. Bifurcation diagrams in the (V, F_z)-plane for different landing gear configurations. a) Original configuration vs. configuration with the NES; b) Original configuration vs. configuration with the PD; c) Original configuration vs. configuration with both PD and NES; d) Comparison among configurations with the NES only, PD only, and both PD and NES. The shaded regions represent the stability domains of the corresponding configurations.

Figure 7b compares the shimmy behavior of the configuration equipped with the PD with that of the original one. The orange-shaded region denotes the instability domain of the PD-equipped configuration, while the black curves correspond to the bifurcation structure of the original system. The bifurcation map shows that the introduction of the particle damper significantly alters the stability structure. Only a single Hopf bifurcation boundary is observed for the PD configuration. However, time-domain analysis indicates that inside this Hopf boundary torsional and lateral bending shimmy occur simultaneously. This region is therefore identified as a “Both” region, where the two shimmy modes coexist.

Furthermore, the PD-only configuration substantially enlarges the instability domain in the low vertical-load range and reduces the minimum vertical load required for shimmy onset. The corresponding onset speed is approximately 15 m/s. Since fixed-wing aircraft typically cannot take off before reaching this speed, the configuration equipped solely with the particle damper is not suitable as an independent shimmy suppression solution.

Figure 7c compares the bifurcation structure of the configuration equipped with both the NES and PD with that of the original configuration. The green curves represent the bifurcation boundaries of the combined NES-PD configuration, whereas the black curves correspond to the original system. The shaded regions denote the stability map of the combined configuration. It can be observed that the torsional shimmy region is significantly reduced compared with that of the original configuration. Moreover, the bistable region almost disappears and remains only in a narrow area near the transition between the pure torsional and lateral bending modes at low forward speeds. This behavior is mainly associated with the modification of the torus bifurcation boundaries in the combined NES-PD configuration, which leads to a pronounced contraction of the bistable region.

From the perspective of shimmy range evolution, the minimum vertical load required for the onset of shimmy increases by 23.6% compared with the original configuration, while the pure torsional shimmy region in the low vertical-load range is reduced by approximately 40%. Meanwhile, the lateral bending shimmy boundary shifts upward by about 5% in terms of vertical load.

Figure 7d compares the configuration with the combined NES and particle damper (PD) with those of the configuration with the NES alone and the configuration with the PD alone. It can be observed that, in the low vertical-load range, the torsional shimmy region of the configuration with the combined PD-NES is essentially identical to that of the configuration with the NES alone, thereby effectively mitigating the adverse effects introduced by the PD-only configuration in this range. Meanwhile, the lateral bending shimmy Hopf boundary of the combined PD-NES configuration is shifted upward by approximately 6.5% in terms of vertical load compared with the NES-only configuration, indicating an improvement in lateral bending shimmy stability. With regard to the distribution of shimmy regions, the modification of the torus bifurcation boundary in the combined PD-NES configuration results in a regime above the torus bifurcation line that is characterized by pure lateral bending shimmy rather than bistable behavior. This feature may be beneficial for subsequent mitigation strategies targeting single-mode oscillations.

In summary, from the perspective of the extent and distribution of shimmy instability regions, the configuration with the NES alone effectively reduces the shimmy region and enlarges the stable domain, particularly in the practically relevant low vertical-load range. In contrast, the configuration with the particle damper alone alters the structure of the stability map and introduces a special region in which torsional and lateral bending shimmy coexist with finite amplitudes, which is therefore identified as a “Both” mode; this change also substantially enlarges the shimmy region at low vertical loads and lowers the shimmy onset threshold. The combined NES-PD configuration retains the advantages of the NES-only case while further improving the stability against lateral bending shimmy.

3.2. Time-Domain Analysis at Representative Operating Points

Based on these observations, nine representative operating points located in different regions of the $(V,\ F_z)$-planes are selected to further examine and compare the performance of the different shimmy suppression strategies, as listed in Table 4. For all time-domain simulations at these representative points, the initial torsional perturbation is set to $\psi = 0.001$ rad, representing a small disturbance condition near the equilibrium state.

Table 4. Shimmy type of selected typical points in (V, F_z)-plane

	(V, F_z)(m s^{-1},kN)	Original	With NES	With PD	With PD and NES
A	(30,150)	Torsion	Torsion	Both	Torsion
B	(110,200)	Torsion	Stable	Both	Stable
C	(170,150)	Stable	Stable	Both	Stable
D	(50,350)	Bistable	Bistable	Both	Lateral
E	(135,350)	Bistable	Lateral	Both	Lateral
F	(180,350)	Lateral	Lateral	Both	Lateral
G	(50,550)	Bistable	Bistable	Both	Lateral
H	(110,550)	Bistable	Lateral	Both	Lateral
I	(170,550)	Lateral	Lateral	Both	Lateral

Note: "Stable" indicates that the system responses decay to the equilibrium state without sustained oscillations under small perturbations. "Torsion" denotes torsional shimmy dominated by torsional oscillations of the landing gear. "Lateral" represents lateral bending shimmy dominated by lateral structural vibration. "Bistable" denotes a bistable regime in which two stable oscillatory solutions coexist, corresponding to torsional shimmy and lateral bending shimmy. "Both" refers to a particle-damper-induced coupled shimmy mode in which both torsional and lateral bending responses exhibit relatively large amplitudes simultaneously.

The selected parameter points are classified into three groups, each corresponding to a distinct vertical load range. Points A - C represent the low vertical-load range, with F_z below 250 kN; points D - F correspond to the medium vertical-load range between 250 kN and 450 kN; and points G - I represent the high vertical-load range above 450 kN. The low-load range associated with points A - C is particularly relevant to aircraft design, as it corresponds to the upper limit of vertical loads that may be encountered in practical operation and also to the range in which torsional shimmy has been observed in several real shimmy incidents. Consequently, the evaluation in this range primarily focuses on the reduction of vibration amplitude and the contraction of the shimmy region, which constitute the main objectives of structural-based shimmy suppression.

The medium vertical-load range represented by points D - F is typically associated with the onset of lateral bending shimmy. Lateral bending shimmy involves bending of the landing gear strut about the aircraft body axis and thus indicates global structural vibration, often referred to as structural shimmy. Such vibrations are highly detrimental and unacceptable in aircraft design due to the risk of structural damage. Therefore, in this load range, particular attention is paid to the occurrence of lateral bending shimmy and to changes in the nature of the instability regions and their evolution trends.

The high vertical-load range corresponding to points G - I generally represents the upper limit of the torsional shimmy Hopf boundary. In this range, a stable torsional Hopf branch may no longer exist in some cases. Analysis in this regime is mainly intended to provide theoretical completeness and to aid in interpreting the qualitative features of the bifurcation structure in the shimmy stability maps.

Figure 8 presents the time-domain responses at points A-C, and Figure 9 illustrates the dominant frequencies in the stable oscillation regions for points A-C.

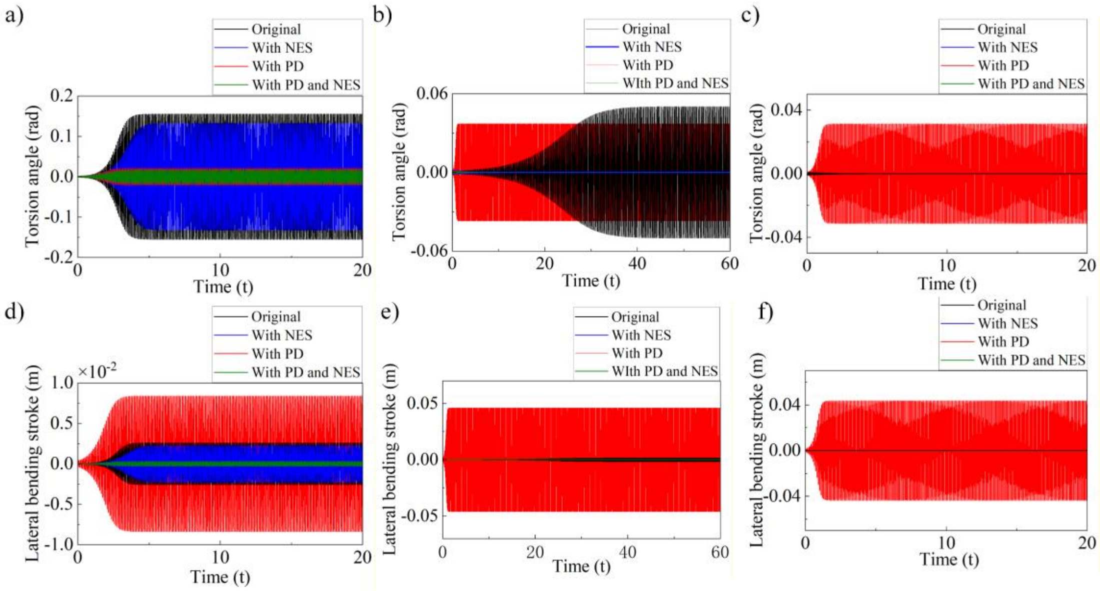

Figure 8. Time histories of the system responses at a) and d): point A; b) and e) point C; c) and f) point C.

Point A is located within the shimmy region for all four landing gear configurations. Among them, the original configuration, the configuration with the NES, and the configuration with both the PD and NES operate in the torsional shimmy region, whereas the configuration with the PD alone exhibits a different behavior. Frequency analysis shows that the dominant frequencies of the original configuration (10.43 Hz), the configuration with the NES (10.61 Hz), and the configuration with both PD and NES (10.88 Hz) are very close, indicating that they correspond to the same vibration mode, namely torsional shimmy. Therefore, this operating point provides a suitable basis for comparing shimmy suppression performance, since these three configurations operate under the same oscillation mode and their effectiveness can be directly evaluated through vibration amplitude.

The time-domain responses at point A clearly reveal the differences in oscillation amplitude. For torsional shimmy, the original configuration exhibits the largest amplitude, approximately 0.156 rad, followed by the configuration with the NES, with an amplitude of about 0.134 rad. In contrast, the two configurations involving the particle damper show a pronounced reduction in torsional amplitude, with values of approximately 0.019 rad for the PD-only configuration and 0.017 rad for the combined PD-NES configuration. The lateral bending responses exhibit a similar trend. The configuration with the PD alone produces the largest lateral bending displacement, about 7.6 mm. The original configuration shows a lateral bending amplitude of about 2.6 mm, slightly larger than that of the configuration with the NES (about 2.3 mm), while the configuration with both PD and NES yields a much smaller displacement of approximately 0.3 mm.

In all cases the responses converge to stable limit-cycle oscillations. The smallest limit cycle occurs for the configuration with both the NES and PD, indicating its superior capability in suppressing vibration amplitude. Overall, the results at point A demonstrate that the combined NES-PD configuration provides the most effective shimmy reduction within the operating conditions represented by this point.

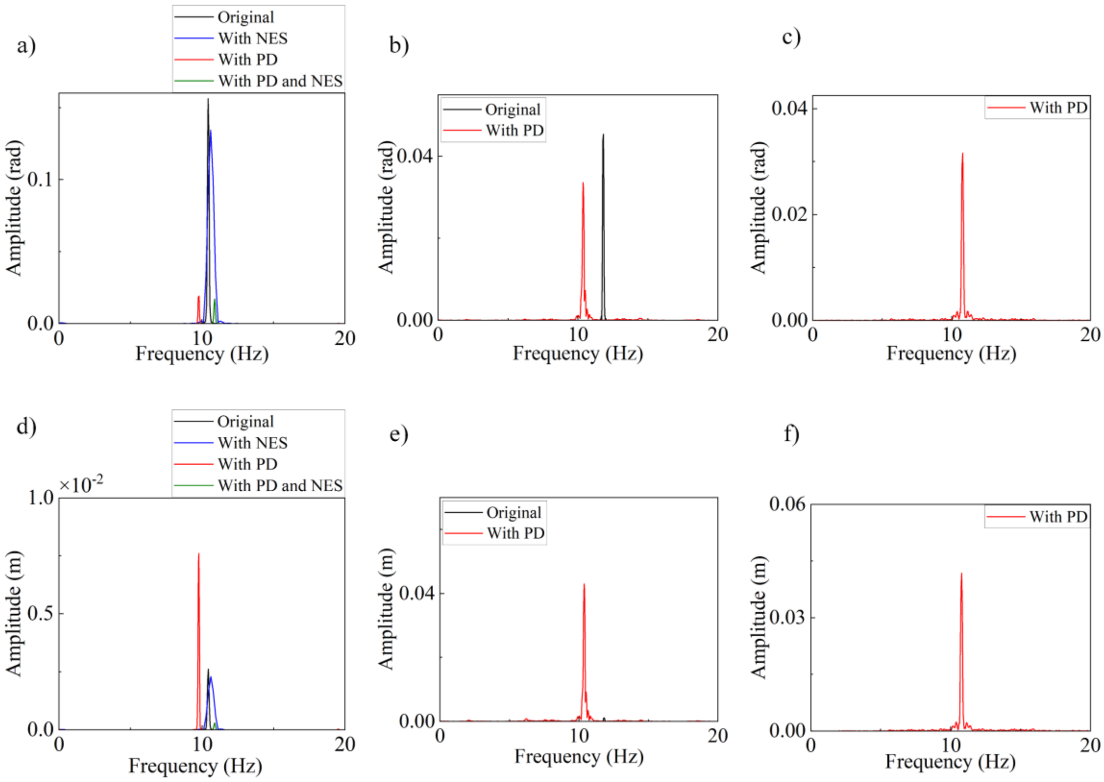

Figure 9. Dominant frequencies of the steady-state responses at a) and d): point A; b) and e) point C; c) and f) point C.

For point B, the configurations with the NES and with both the NES and PD remain stable and do not exhibit shimmy, with the responses rapidly converging to the equilibrium state under small perturbations. In contrast, the configuration with the PD alone exhibits large oscillations in both the torsional and lateral bending responses, indicating the coexistence of the two vibration modes. The original configuration eventually develops a steady torsional shimmy after a relatively long transient, while the lateral bending displacement remains negligible, which is characteristic of pure torsional shimmy. Although the PD-only configuration reduces the torsional shimmy amplitude by about 25% compared with the original configuration, it also produces a pronounced increase in the lateral bending response, with a displacement of approximately 4.3 mm. This behavior indicates the emergence of a distinct oscillatory regime induced by the particle damper. In this regime, both the torsional and lateral bending responses exhibit relatively large amplitudes simultaneously, rather than being dominated by a single shimmy mode. This PD-induced coupled oscillation mode is therefore referred to as the “Both” mode.

At point C, shimmy occurs only for the configuration with the PD alone, while the other three configurations remain stable. The dominant frequency of this oscillation is approximately 10.78 Hz, which is close to that observed at point B (10.36 Hz), indicating that the same shimmy mode persists. For the remaining configurations, the responses decay rapidly to the equilibrium state without sustained oscillations.

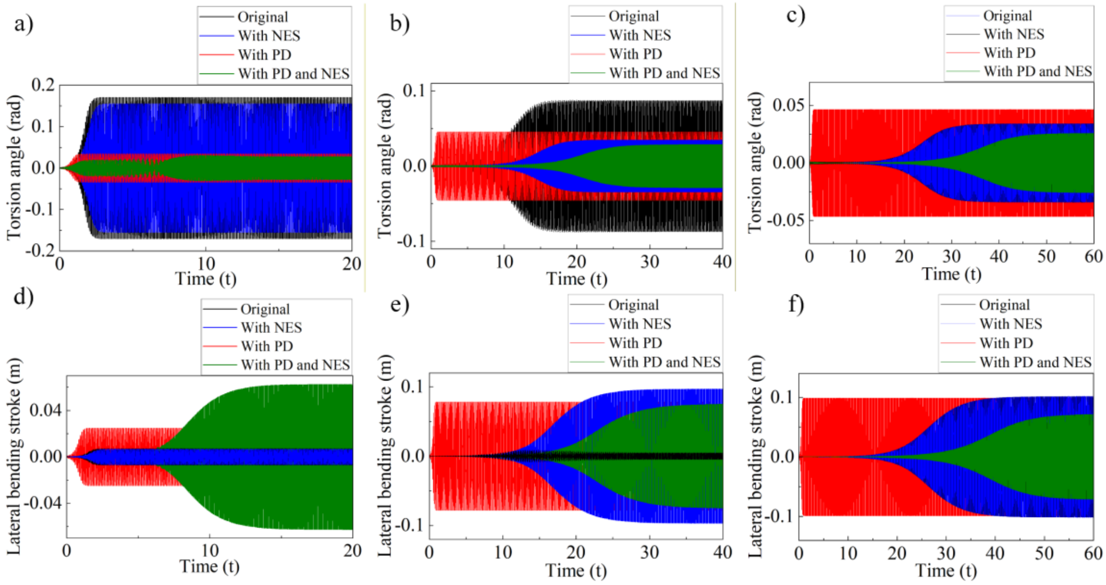

Figure 10. Time histories of the system responses at a) and d): point D; b) and e) point E; c) and f) point F.

Points D, E, and F are representative operating points located in the medium vertical-load range and lie above the lateral bending Hopf bifurcation boundary for the configurations where such a boundary exists. Therefore, lateral bending shimmy is expected to occur to some extent in this region. Figure 10 shows the corresponding time-domain responses, while Figure 11 presents the dominant frequencies of the steady-state responses.

Point D lies in the “Both” mode region for the PD-only configuration. The original configuration and the configuration with the NES are located in the bistable region, where the responses may converge to either torsional or lateral bending shimmy. In contrast, the combined PD-NES configuration falls within the lateral bending shimmy region. From the time-domain responses, the torsional amplitudes of the original configuration (0.168 rad) and the configuration with the NES (0.157 rad) remain relatively large, whereas the configurations involving the particle damper show much smaller amplitudes, namely 0.033 rad for the PD-only configuration and 0.025 rad for the combined PD-NES configuration. The combined PD-NES configuration exhibits a transient growth during the first 10 s and subsequently stabilizes into a lateral bending shimmy with a displacement of approximately 0.05 m. The frequency spectra further confirm these behaviors. The combined PD-NES configuration exhibits a dominant frequency of 16.09 Hz, which is characteristic of lateral bending shimmy. For the original configuration and the configuration with the NES, the dominant frequencies are 11.81 Hz and 11.11 Hz, respectively, indicating that the responses are influenced by lateral bending dynamics.

At point E, the original configuration lies within the bistable region, whereas the configurations with the NES alone and with the combined PD-NES fall into the lateral bending shimmy region. The PD-only configuration operates in its characteristic “Both” mode region. The original configuration, although located in the bistable region, exhibits a response dominated by torsional shimmy. In contrast, the configurations with the NES and with the combined PD-NES gradually evolve toward lateral bending shimmy after a transient process of about 30 s. The dominant frequencies of these two configurations are 16.06 Hz and 16.08 Hz, respectively, which are typical of lateral bending shimmy. The original configuration exhibits a dominant frequency of 12.52 Hz, indicating that the response is influenced by lateral bending dynamics while remaining within the bistable regime. The PD-only configuration shows a dominant frequency of 10.40 Hz, consistent with the previously identified "Both" mode.

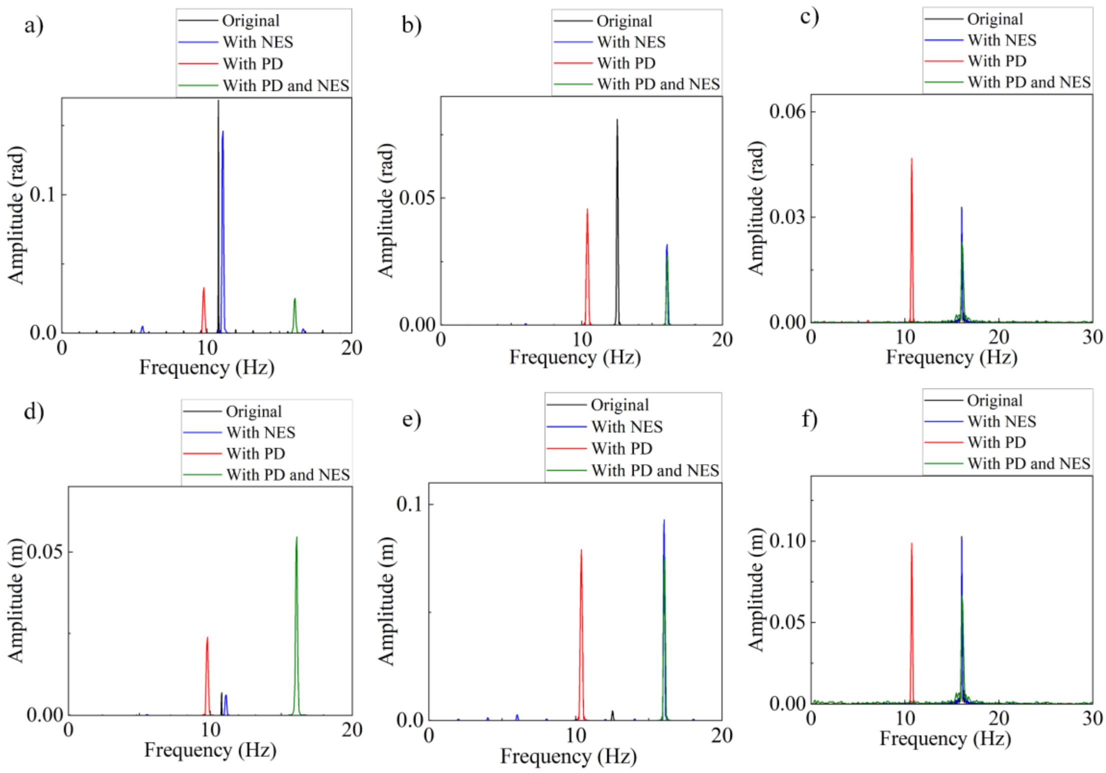

Figure 11. Dominant frequencies of the steady-state responses at a) and d): point D; b) and e) point E; c) and f) point F.

Point F corresponds to a region where lateral bending shimmy dominates for all configurations except the PD-only configuration. The PD-only configuration continues to operate in the "Both" mode, while the other three configurations exhibit the same lateral bending shimmy mode. The frequency analysis confirms this observation. The dominant frequencies are approximately 16.04 Hz for the original configuration, 16.04 Hz for the configuration with the NES, and 16.06 Hz for the configuration with both the NES and PD, indicating that all three operate in the lateral bending shimmy mode. This allows a direct comparison of the lateral bending amplitudes under identical modal conditions. The time-domain responses show that the lateral bending amplitude of the original configuration is about 0.103 m, which is slightly larger than that of the configuration with the NES (about 0.101 m), while the configuration with both the NES and PD exhibits a significantly smaller amplitude of approximately 0.067 m. Although lateral bending shimmy is structurally undesirable and unacceptable in practical applications, this comparison still provides a useful reference for evaluating the relative suppression performance. Among the three cases, the combined PD-NES configuration again demonstrates the best performance by producing the smallest lateral bending amplitude.

The final group corresponds to the representative points G, H, and I located in the high vertical-load range. Figure 12 presents the time-domain responses and Figure 13 provides the frequency analysis for these points.

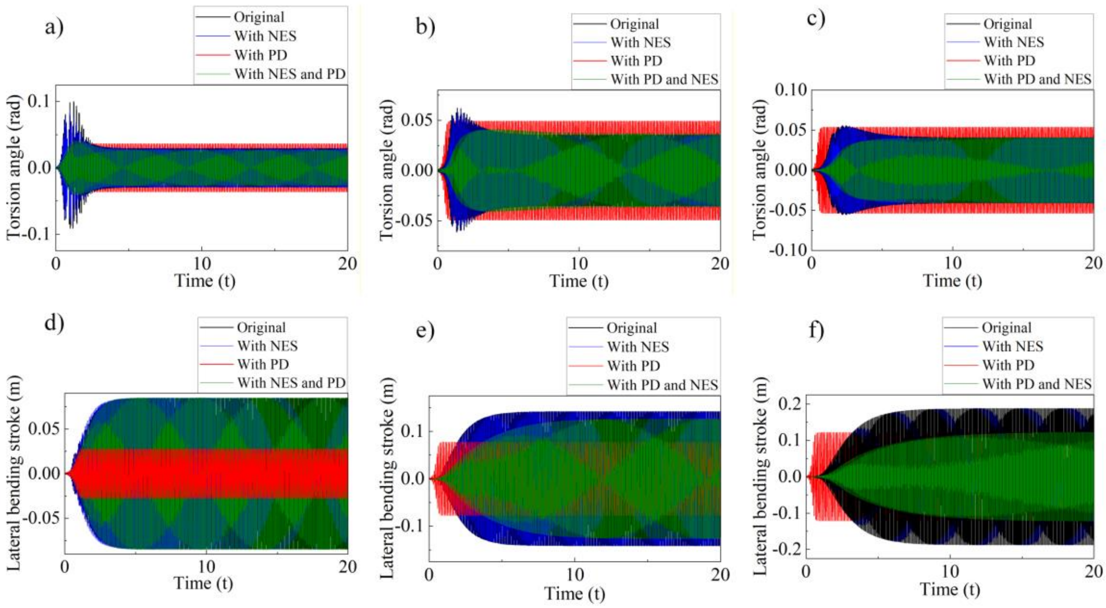

Figure 12. Time histories of the system responses at a) and d): point G; b) and e) point H; c) and f) point I.

Point G is examined next. In this case, the original configuration and the configuration with the NES lie within the bistable regime, whereas the combined PD-NES configuration falls into the lateral bending shimmy region. The PD-only configuration remains in its characteristic "Both" mode region. The time-domain responses show that the original configuration and the configuration with the NES eventually converge to periodic oscillations associated with lateral bending shimmy. In contrast, the combined PD-NES configuration directly evolves toward a lateral bending shimmy state with a relatively smooth transition. The steady-state frequency analysis further supports these observations. For the original configuration and the configuration with the NES, the dominant frequencies fall within the typical range of lateral bending shimmy, indicating that the steady-state responses in the bistable region are governed by lateral bending dynamics. The PD-only configuration exhibits a dominant frequency of 9.71 Hz, which corresponds to the previously identified "Both" mode. The verification of torsional shimmy at higher vertical loads is further examined through the one-parameter bifurcation analysis presented in Figure 14.

For point H, the original configuration remains in the bistable region, whereas the configurations with the NES and with the combined PD-NES lie in the transition region toward lateral bending shimmy. The PD-only configuration again operates in the "Both" mode region. The time-domain responses indicate that the original configuration ultimately converges to a lateral bending shimmy response. Similarly, the configurations with the NES alone and with the combined PD-NES also evolve toward lateral bending shimmy. The steady-state frequency analysis confirms that, except for the PD-only configuration, which exhibits a dominant frequency of about 10.03 Hz, the remaining three configurations operate at frequencies characteristic of lateral bending shimmy.

At point I, all configurations except the PD-only configuration are located within the lateral bending shimmy region. The time-domain responses show that the original configuration, the configuration with the NES, and the configuration with the combined PD-NES all converge to stable lateral bending shimmy oscillations. The dominant frequencies extracted from the steady-state responses further confirm that these three configurations operate within the characteristic frequency range of lateral bending shimmy. In contrast, the PD-only configuration exhibits a dominant frequency of approximately 10.39 Hz, which corresponds to the previously identified “Both” mode.

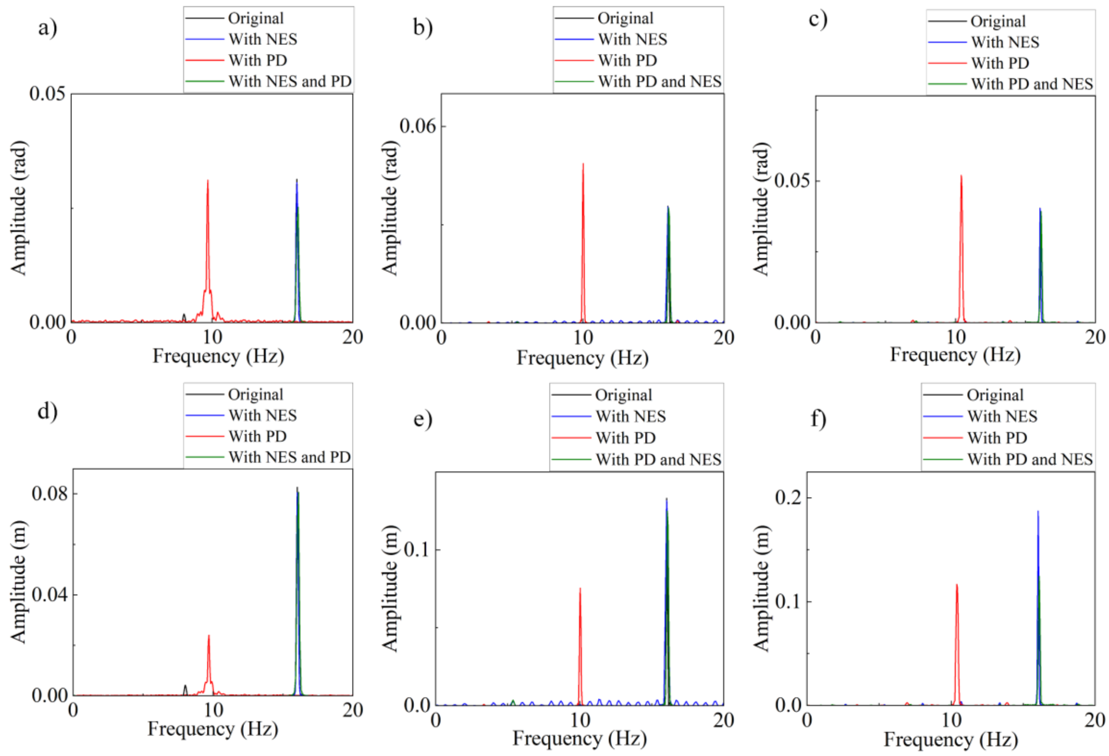

Figure 13. Dominant frequencies of the steady-state responses at a) and d): point G; b) and e) point H; c) and f) point I.

In the high vertical-load region corresponding to points G, H, and I, the dominant frequencies of all configurations except the PD-only case fall within the characteristic range of lateral bending shimmy, indicating that the steady-state responses obtained from time-domain simulations are governed by the lateral bending mode. However, the time-domain results alone cannot determine whether the torsional shimmy mode still exists as another stable attractor in this parameter region.

To examine this possibility, a one-parameter bifurcation analysis with respect to the forward speed is carried out at a vertical load of $F_z = 850$ kN, which lies above both the torsional Hopf loop and the torus bifurcation boundaries. The results for the configuration with the NES are shown in Figs. 14a and 14c, while the corresponding results for the original configuration are presented in Figs. 14b and 14d. As illustrated in these figures, since the analysis is conducted beyond the torsional Hopf loop, the solution branches originate from the saddle-node bifurcation of periodic orbits. When the forward speed exceeds the left saddle-node bifurcation boundary, a stable branch with relatively large torsional amplitudes emerges. As the speed further increases, this stable branch disappears at the right saddle-node bifurcation boundary. By comparing the maximum amplitudes in Figs. 14a and 14c with those in Figs. 14b and 14d, it can be confirmed that this stable branch corresponds to a torsional shimmy mode. These results demonstrate that, even above the torsional Hopf loop and the torus bifurcation boundaries in the (V, F_z)-plane, both the original configuration and the configuration equipped with the NES retain stable torsional shimmy solutions. The onset and termination of these torsional responses are governed by the two saddle-node bifurcation curves, thereby validating the region classification obtained from the (V, F_z)-plane bifurcation analysis.

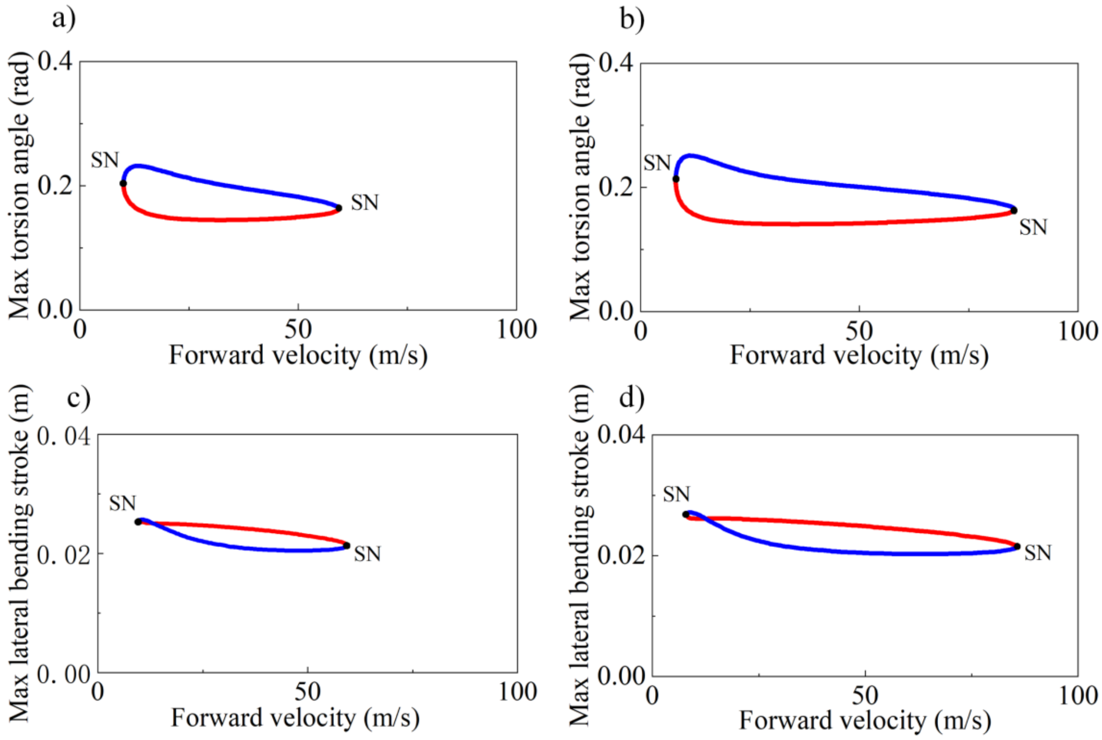

Figure 14. One-parameter bifurcation analysis with respect to forward speed at $F_z = 850$ kN). a) and c) correspond to the configuration with the NES while b) and d) correspond to the original configuration. Stable and unstable solution branches are indicated by blue and red curves, respectively.

3.3. One-parameter bifurcation analysis with respect to forward speed

Based on the analysis of the nine representative points spanning different regions of the (V, F_z)-plane, the validity of the bifurcation results can be confirmed, and the dynamical characteristics associated with each region can be clearly identified. However, in the low vertical-load range, which corresponds to the load levels that may realistically be encountered in actual aircraft operation, the behavior inferred from a limited number of discrete points can only provide a local assessment and cannot fully describe the shimmy evolution and vibration amplitude throughout the entire takeoff and landing process. Therefore, a one-parameter bifurcation analysis with respect to the forward speed V is further introduced to compare the shimmy behavior and vibration amplitude of the four configurations in the low-load range as the speed varies. This approach allows a more direct and intuitive evaluation of the key performance characteristics of the proposed shimmy suppression strategies under realistic operating scenarios, as illustrated in the Figure 15.

A representative vertical load of 150 kN is selected for this analysis. In this low-load range, shimmy is dominated primarily by pure torsional oscillations; therefore, the torsional angle range and the maximum torsional amplitude are adopted as the key criteria for comparing the performance of the four configurations. As shown in the Figure 15, the original configuration without any suppression device exhibits the largest maximum torsional amplitude among all cases, reaching about 0.215 rad, and it also presents a relatively wide torsional shimmy range. The onset of shimmy occurs at a forward speed of 5.61 m/s and terminates at approximately 93.43 m/s. For the configuration with the NES, both the vibration amplitude and the shimmy region are reduced compared with the original case. The maximum torsional amplitude decreases to about 0.177 rad, while the shimmy onset speed increases to 6.73 m/s and the termination speed decreases to 71.25 m/s. For the configuration with the PD alone, a pronounced suppression of the torsional shimmy amplitude is observed, with a maximum torsional angle of about 0.041 rad. However, the corresponding shimmy region is extremely wide. Within the investigated speed range, only the onset point at 14.19 m/s is visible. Owing to the supercritical nature of the Hopf bifurcation, a second Hopf point defining the upper boundary of the shimmy region should exist at much higher speeds, which is estimated to be on the order of 1500 m/s and is therefore not shown in the figure. For the configuration with both the PD and the NES, the advantages of the two devices are effectively combined. This configuration exhibits both the low vibration amplitude characteristic of the PD and the reduced shimmy region associated with the NES. The maximum torsional amplitude is further reduced to about 0.022 rad, while the shimmy onset and termination speeds are approximately 6.41 m/s and 71.95 m/s, respectively.

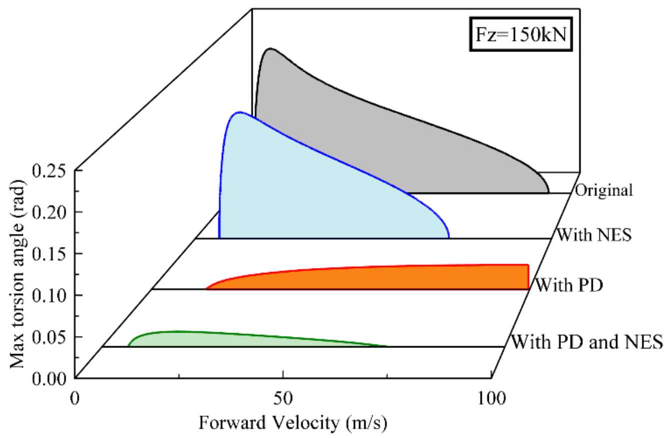

Figure 15. One-parameter bifurcation results versus forward speed at $F_z = 150\text{kN}$ for the four landing gear configurations.

A comparison of the results in the low vertical-load range indicates that, within the load levels relevant to current aircraft landing gear operation, where the response is mainly composed of pure torsional shimmy and stable regions, the configuration with both the PD and the NES provides superior shimmy performance. Compared with the original configuration, it achieves a substantial reduction in vibration amplitude of about 87% and a moderate contraction of the shimmy region of approximately 25%. The configuration with the NES alone also exhibits improved shimmy characteristics relative to the original case.

4. Parametric analysis of the shimmy suppression devices

Based on the results presented in the previous section, the landing gear configuration equipped with both the PD and the NES exhibits superior shimmy suppression performance, while the configuration with the NES alone also demonstrates relatively favorable behavior. Therefore, this section focuses on a parametric analysis of key design parameters associated with the NES and the PD, with the aim of providing guidance for practical parameter selection and design of shimmy suppression devices.

4.1. Parametric analysis of the NES

Four design parameters of the NES are considered as independent variables: the radius of the concave track r_2, the spring pre-stretch e_p, the spring stiffness k_s, and the radius of the inner roller r_3. In the analysis involving the combined NES-PD configuration, the parameters of the particle damper are kept constant to isolate the effects of the NES parameters.

The first parameter examined is the concave track radius r_2, and the three values $r_2 = 0.09$ m, 0.08 m and 0.07 m are selected. From a structural design perspective, r_2 primarily governs the nonlinear stiffness characteristics of the NES. Since the engagement angle between the concave track and the main shaft is fixed at $\pi/3$, a larger value of r_2 corresponds to a smaller effective engagement arc, resulting in weaker nonlinear stiffness. The corresponding results are presented in Table 5.

Table 5. Shimmy characteristics for different concave track radii r_2 in the NES-only and combined PD-NES configurations.

	r_2 (m)	Start Hopf point (m/s)	End Hopf point (m/s)	Max amplitude (rad)
With NES	0.09	6.725	71.307	0.178
	0.08	6.730	71.255	0.177
	0.07	6.736	71.191	0.176
With NES and PD	0.09	6.404	72.006	0.019
	0.08	6.410	71.952	0.019
	0.07	6.414	71.885	0.019

For the NES-only configuration, a reduction in r_2 delays the onset of shimmy and advances the termination point, thereby narrowing the speed range over which shimmy occurs. In addition, a slight reduction in shimmy amplitude is observed as r_2 decreases. The combined NES-PD configuration exhibits a similar trend in terms of the shrinkage of the shimmy region. However, with respect to vibration amplitude, variations in r_2 have only a limited influence on the overall shimmy response.

The influence of the spring pre-stretch e_p is examined next, by considering $e_p = 0.005$ m, $e_p = 0.01$ m, and $e_p = 0.0005$ m. From a structural standpoint, the pre-stretch is positively correlated with the linear stiffness of the NES, which increases as the pre-stretch is enlarged. In contrast, the effect of the pre-stretch on the nonlinear stiffness component is relatively weak, as illustrated by the results shown in Figure 20.

Figure 16 presents the shimmy response curves corresponding to the three values of e_p for both the NES-only and the combined NES-PD configurations, and the quantitative results are summarized in Table 6. The data clearly indicate that increasing the pre-stretch reduces both the speed range over which shimmy occurs and the associated vibration amplitude. A similar trend is observed for the configuration with both the NES and PD. It should be noted, however, that increasing the pre-stretch primarily enhances the linear stiffness while having a limited influence on the nonlinear stiffness, which may introduce additional resonance or bifurcation phenomena, such as internal resonances, due to the increased linear stiffness.

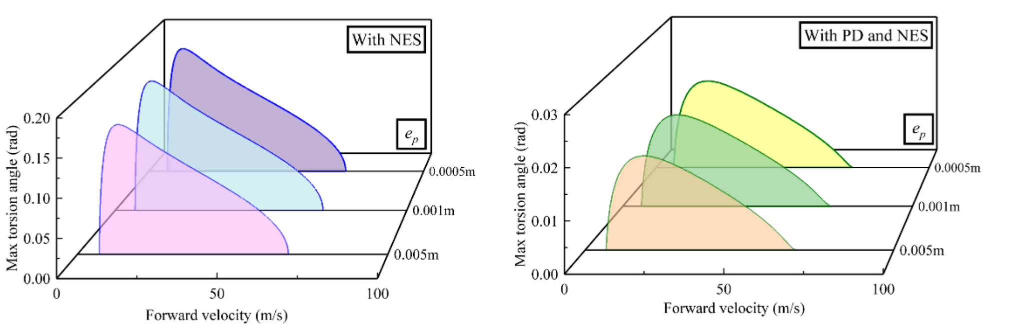

Figure 16. Influence of the spring pre-stretch e_p on shimmy performance for the NES-only and combined PD-NES configurations.

Table 6. Shimmy characteristics for different spring pre-stretch values e_p in the NES-only and combined PD-NES configurations.

	e_p (m)	Start Hopf point (m/s)	End Hopf point (m/s)	Max amplitude (rad)
With NES	0.005	7.050	67.939	0.167
	0.001	6.730	71.255	0.177
	0.0005	6.697	71.629	0.178
With NES and PD	0.005	6.725	68.484	0.018
	0.001	6.410	71.952	0.019
	0.0005	6.377	72.342	0.019

The effect of the spring stiffness k_s is examined next. The spring stiffness is positively correlated with both the linear and nonlinear stiffness components of the NES; as k_s increases, the stiffness contributions of both the linear term and the nonlinear term are enhanced. Three representative stiffness values are selected for the analysis, namely $k_s = 1.0 \times 10^6$, 1.2×10^6, and 1.4×10^6.

The quantitative results for the two configurations are summarized in Table 7. It can be observed that, for both configurations, increasing the spring stiffness leads to a contraction of the shimmy region and a reduction in vibration amplitude. However, the spring stiffness cannot be increased without limitation. On the one hand, material and structural constraints impose practical upper bounds. On the other hand, an excessive increase in torsional stiffness may promote structural shimmy in the form of lateral bending oscillations, which is undesirable from a design standpoint.

Table 7. Shimmy characteristics for different spring stiffness values k_s in the NES-only and combined PD-NES configurations.

	k_s (N/m)	Start Hopf point (m/s)	End Hopf point (m/s)	Max amplitude (rad)
With NES	1.0×10^6	6.719	71.380	0.178
	1.2×10^6	6.730	71.255	0.177

	1.4×10^6	6.741	71.128	0.176
With NES and PD	1.0×10^6	6.398	72.083	0.019
	1.2×10^6	6.410	71.952	0.019
	1.4×10^6	6.420	71.820	0.019

Finally, the influence of the inner roller radius r_3 is investigated. r_3 is positively correlated with the linear stiffness to a certain extent, since an increase in the roller radius is partially equivalent to an increase in the effective pre-stretch. At the same time, r_3 also affects the nonlinear stiffness, because the roller radius modifies the curvature variation experienced by the roller along the internal track, thereby influencing the nonlinear stiffness component. Three representative values, $r_3 = 0.02$ m, 0.01 m, and 0.005 m, are selected, and the quantitatively summarized in Table 8.

Table 8. Shimmy characteristics for different inner roller radii r_3 in the NES-only and combined PD-NES configurations.

	r_3 (N/m)	Start Hopf point (m/s)	End Hopf point (m/s)	Max amplitude (rad)
With NES	0.02	6.714	71.433	0.179
	0.01	6.730	71.255	0.177
	0.005	6.739	71.149	0.176
With NES and PD	0.02	6.393	72.137	0.019
	0.01	6.410	71.952	0.019
	0.005	6.418	71.842	0.019

It can be observed that a reduction in the roller radius r_3 improves shimmy suppression performance by contracting the shimmy region. It should be noted, however, that r_3 corresponds to the roller mounted within the internal track and therefore cannot be reduced arbitrarily; its value must be selected within a limited and practically feasible range.

Overall, the results of this subsection indicate that the two configurations exhibit similar trends with respect to parameter variations. Increasing the concave track radius r_2 and the inner roller radius r_3 tends to degrade shimmy suppression performance, whereas increasing the spring pre-stretch e_p and the spring stiffness k_s generally enhances the shimmy suppression capability of the structure. However, within the considered parameter ranges, the magnitude of these adjustments is relatively limited. As a result, the variations mainly reveal the general trends of the system response rather than producing substantial changes in the overall shimmy behavior.

4.2. Parametric analysis of the PD

This subsection focuses on the structural parameters of the particle damper. In Section 3 it has been shown that a configuration equipped with the PD alone is not suitable for effective shimmy suppression in landing gear systems. In contrast, the combined configuration incorporating both the NES and the PD provides effective mitigation of shimmy. Therefore, the present analysis is restricted to the landing gear configuration equipped with both the NES and the PD.

The parameters varied in this study are the particle filling ratio a_p and the particle material, which together determine the effective particle density and thus influence the damping performance.

These parameters are selected because they can be conveniently adjusted in practical implementations without modifying the primary structural configuration of the particle damper. In other words, changes in particle loading or particle material can be achieved while maintaining the overall geometry and structural design of the damper. During this analysis, the parameters of the NES are kept unchanged.

As shown in the left panel of Figure 17, different particle filling ratios have a limited influence on the shimmy region. Increasing the filling ratio leads to a slight contraction of the shimmy region, but the overall effect remains relatively small. In contrast, the filling ratio has a more pronounced impact on the vibration amplitude. For example, increasing the filling ratio from 0.8 to 0.9 results in an amplitude reduction of approximately 10%. This indicates that the primary contribution of the PD lies in amplitude attenuation rather than in a substantial reduction of the instability region.

The influence of particle material is more evident in the right panel of Figure 17. Although the configurations using steel particles and tungsten powder exhibit similar shimmy regions, a clear difference in vibration amplitude can be observed. This behavior can be attributed to the higher particle density of tungsten powder compared with steel particles when other parameters are kept the same, leading to enhanced damping effectiveness.

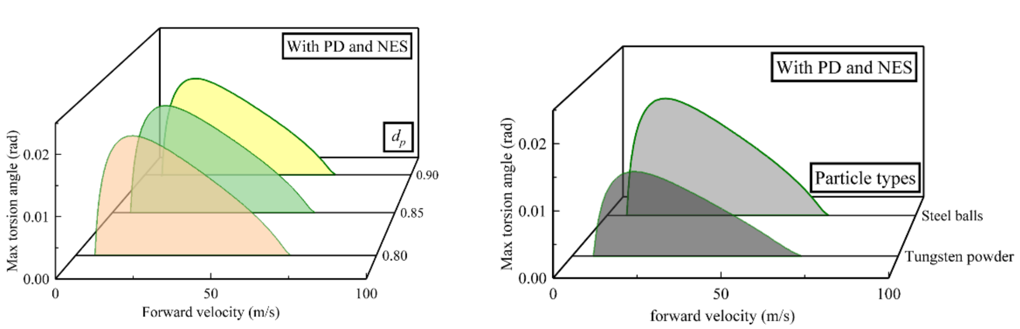

Figure 17. Influence of particle filling ratio and particle material on shimmy performance for the combined PD-NES configuration.

Conclusion

This paper investigated the shimmy dynamics and vibration suppression performance of a single-wheel nose landing gear by integrating a torsional nonlinear energy sink (NES) and an annular granular particle damper (PD). A nonlinear shimmy model considering coupled torsional and lateral bending modes was established based on the Thota tire formulation and the stretched-string tire deformation dynamics. The proposed torsional NES was designed from a modified roller–spring mechanism, and its nonlinear restoring torque was derived through geometric analysis and Taylor expansion, exhibiting a near-zero linear stiffness with a positive cubic stiffness component. The annular PD was modeled using a gas-solid two-phase-flow-based equivalent viscous damping approach, and the resulting torsional damping torque was incorporated into the shimmy equations.

Bifurcation analyses were performed using MATCONT in the $(V,\ F_z)$-plane to evaluate the stability boundaries and the occurrence regions of torsional shimmy, lateral bending shimmy, and bistable oscillations. The results indicate that:

i) the standalone torsional NES effectively reduces the torsional shimmy region and enlarges the stable domain in the practically relevant low-load range, increasing the minimum vertical load triggering shimmy by approximately 22.6% and reducing the pure torsional shimmy region by about 35%;

ii) The standalone PD significantly suppresses torsional vibration amplitude but simultaneously enlarges the shimmy region toward lower speeds and induces a characteristic “Both” oscillation mode, in which torsional and lateral bending responses exhibit relatively large amplitudes simultaneously. This behavior suggests that the PD alone is not suitable as an independent shimmy suppression solution;

iii) the combined NES-PD configuration preserves the region-shrinking benefit of the NES while further improving the overall suppression performance, increasing the minimum vertical load for shimmy by about 23.6% and reducing the low-load pure torsional shimmy region by about 40%. Moreover, in the representative low-load case ($F_z = 150$ kN), the combined configuration achieves a substantial reduction in maximum torsional amplitude (about 87% compared with the reference case) while maintaining a reduced shimmy speed interval.

A parametric study further revealed the design sensitivity of the NES and PD. For the NES, decreasing the concave track radius r_2 and the roller radius r_3 improves shimmy suppression by narrowing the unstable speed range, whereas increasing the spring pre-stretch e_p and stiffness k_s generally enhances suppression but may introduce additional stiffness effects if excessively increased. For the PD, increasing the filling ratio and adopting higher-density particles mainly contribute to amplitude attenuation, and they also lead to a slight contraction of the shimmy region for the combined NES-PD system; however, this region-reduction effect is relatively small, indicating that the PD plays a secondary role in shrinking the instability domain compared with the NES.

Overall, the proposed NES-PD hybrid concept provides an effective passive strategy for reducing shimmy amplitude and limiting the unstable operating region, which is particularly attractive for heavy-load landing gear applications. These findings provide useful guidelines for the practical design of passive shimmy suppression devices in advanced landing gear systems.

Reference

[1] Neumaier, M., Schopper, C., Gundlach, T., Gast, C., Döring, D., and Rudolph, S., 2024, “Automated Packing and Piping in an Airbus A320 Main Landing Gear Bay: An Industrial Development Case Study,” CEAS Aeronaut. J. https://doi.org/10.1007/s13272-024-00765-3.

[2] S Norman, 1989, “Aircraft Landing Gear Design: Principles and Practices,” Aeronautical journal, **93**(929), p. 361. https://doi.org/10.1017/S0001924000017310.

[3] Arreaza, C., Behdinan, K., and Zu, J. W., 2016, “Linear Stability Analysis and Dynamic Response of Shimmy Dampers for Main Landing Gears,” Journal of Applied Mechanics, Transactions ASME, **83**(8). https://doi.org/10.1115/1.4033482.

[4] Li, Y., Howcroft, C., Neild, S. A., and Jiang, J. Z., 2017, “Using Continuation Analysis to Identify Shimmy-Suppression Devices for an Aircraft Main Landing Gear,” J. Sound Vib., **408**, pp. 234-251. https://doi.org/10.1016/j.jsv.2017.07.028.

[5] Howcroft, C., Lowenberg, M., Neild, S., Krauskopf, B., and Coetzee, E., 2015, “Shimmy of an Aircraft Main Landing Gear with Geometric Coupling and Mechanical Freeplay,” J.

Comput. Nonlinear Dyn., **10**(5). https://doi.org/10.1115/1.4028852.

[6] Thota, P., Krauskopf, B., and Lowenberg, M., 2009, "Interaction of Torsion and Lateral Bending in Aircraft Nose Landing Gear Shimmy," Nonlinear Dyn., **57**(3), pp. 455-467. https://doi.org/10.1007/s11071-008-9455-y.

[7] Somieski, G., 1997, "Shimmy Analysis of a Simple Aircraft Nose Landing Gear Model Using Different Mathematical Methods," Aerosp. Sci. Technol., **1**(8), pp. 545-555. https://doi.org/10.1016/S1270-9638(97)90003-1.

[8] Rahmani, M., and Behdinan, K., 2019, "Investigation on the Effect of Coulomb Friction on Nose Landing Gear Shimmy," Journal of Vibration and Control, **25**(2), pp. 255-272. https://doi.org/10.1177/1077546318774440.

[9] Rahmani, M., and Behdinan, K., 2019, "Parametric Study of a Novel Nose Landing Gear Shimmy Damper Concept," J. Sound Vib., **457**, pp. 299-313. https://doi.org/10.1016/j.jsv.2019.06.008.

[10] Rahmani, M., and Behdinan, K., 2019, "On the Effectiveness of Shimmy Dampers in Stabilizing Nose Landing Gears," Aerosp. Sci. Technol., **91**, pp. 272-286. https://doi.org/10.1016/j.ast.2019.05.040.

[11] Mustashin, M. S., Rahmani, M., and Behdinan, K., 2021, "Experimental Characterization of a Novel Nose Landing Gear Shimmy Damper Using a Small-Scale Test Rig," Aerosp. Sci. Technol., **112**. https://doi.org/10.1016/j.ast.2021.106625.

[12] Feng, G., Jiang, B., and Jiang, Y., 2023, "Effect of Multi-Joint Clearance Coupling on Shimmy of Nose Landing Gear," Aerospace, **10**(11). https://doi.org/10.3390/aerospace10110911.

[13] Jiang, Y., Feng, G., Tang, H., Zhang, J., and Jiang, B., 2023, "Effect of Coulomb Friction on Shimmy of Nose Landing Gear under Time-Varying Load," Tribol. Int., **188**. https://doi.org/10.1016/j.triboint.2023.108828.

[14] Du, X., Xu, Y., Liu, Q., Liu, C., Yue, X., Liu, X., and Kurths, J., 2024, "Shimmy Dynamics in a Dual-Wheel Nose Landing Gear with Freeplay under Stochastic Wind Disturbances," Nonlinear Dyn., **112**(4), pp. 2477-2499. https://doi.org/10.1007/s11071-023-09182-3.

[15] Gao, X., Zheng, Y., Du, X., Shan, Z., Jia, B., and Lu, X., 2024, "Effect of Clearance Position of Torque Link Structure on Nose Landing Gear Shimmy," Int. J. Non. Linear. Mech., **159**. https://doi.org/10.1016/j.ijnonlinmec.2023.104616.

[16] Thota, P., Krauskopf, B., and Lowenberg, M., 2010, "Bifurcation Analysis of Nose-Landing-Gear Shimmy with Lateral and Longitudinal Bending," *Journal of Aircraft*, American Institute of Aeronautics and Astronautics Inc., pp. 87-95. https://doi.org/10.2514/1.43507.

[17] Thota, P., Krauskopf, B., and Lowenberg, M., 2012, "Multi-Parameter Bifurcation Study of Shimmy Oscillations in a Dual-Wheel Aircraft Nose Landing Gear," Nonlinear Dyn., **70**(2), pp. 1675-1688. https://doi.org/10.1007/s11071-012-0565-1.

[18] Thota, P., Krauskopf, B., Lowenberg, M., and Coetzee, E., 2010, "Influence of Tire Inflation Pressure on Nose Landing Gear Shimmy," J. Aircr., **47**(5), pp. 1697-1706. https://doi.org/10.2514/1.C000248.

[19] Jiang, Y., Sun, J., Zhong, S., and Jiang, B., 2025, "Nose Landing Gear Shimmy Analysis with Variable System Stiffness Under Time-Varying Load," Aerospace, **12**(10). https://doi.org/10.3390/aerospace12100926.

[20] Ruan, S., Zhang, M., Shi, X., Liu, X., and Nie, H., 2025, "Stability Analysis of Shimmy

under the Consideration of Tire Pavement Contact Mechanics Behavior," J. Sound Vib., **600**. https://doi.org/10.1016/j.jsv.2024.118916.

[21] Wu, C., Li, S., and Yang, F., 2025, "Analysis of Nose Landing Gear Shimmy Based on Multi-Body Dynamics Simulations," *Journal of Physics: Conference Series*, Institute of Physics. https://doi.org/10.1088/1742-6596/3078/1/012023.

[22] Liu, Y., Mojahed, A., Bergman, L. A., and Vakakis, A. F., 2019, "A New Way to Introduce Geometrically Nonlinear Stiffness and Damping with an Application to Vibration Suppression," Nonlinear Dyn., **96**(3), pp. 1819-1845. https://doi.org/10.1007/s11071-019-04886-x.

[23] Chen, Y., Yang, J.-H., Nan, T., Yang, X.-D., Lu, K., and Liang, F., 2026, "Advances in Dynamics of Fluid-Conveying Pipes: Model, Strategy and Experiment," Int. J. Mech. Sci., **312**, p. 111241. https://doi.org/10.1016/j.ijmecsci.2026.111241.

[24] Sanches, L., Guimarães, T. A. M., and Marques, F. D., 2021, "Nonlinear Energy Sink to Enhance the Landing Gear Shimmy Performance," Acta Mech., **232**(7), pp. 2605-2622. https://doi.org/10.1007/s00707-021-02985-8.

[25] Guo, W., Xu, Y., Liu, Q., Lenci, S., and Li, G., 2024, "Reliability of Hypersonic Airfoil with Freeplay and Stochasticity via Nonlinear Energy Sink," AIAA Journal, **62**(9), pp. 3258-3270. https://doi.org/10.2514/1.J064048.

[26] Wang, Y., Zhang, T., Yin, Y., and Wei, X., 2024, "Reducing Shimmy Oscillation of a Dual-Wheel Nose Landing Gear Based on Torsional Nonlinear Energy Sink," Nonlinear Dyn., **112**(6), pp. 4027-4062. https://doi.org/10.1007/s11071-023-09267-z.

[27] Wang, Y., Zhang, T., Jin, X., and Yin, Y., 2023, "Shimmy Suppression of an Aircraft Nose Landing Gear Using Torsional Nonlinear Energy Sink," J. Comput. Nonlinear Dyn., **18**(10). https://doi.org/10.1115/1.4062909.

[28] Friskney, B., Alevras, P., Londhe, S., Theodossiades, S., and McFarland, D. M., 2022, "A Nonlinear Energy Sink Design to Attenuate the Torsional Oscillations of Lightly Loaded Gear Pairs," Applied Sciences (Switzerland), **12**(13). https://doi.org/10.3390/app12136778.

[29] Duan, N., Wu, Y., Sun, X. M., and Zhong, C., 2021, "Vibration Control of Conveying Fluid Pipe Based on Inerter Enhanced Nonlinear Energy Sink," IEEE Transactions on Circuits and Systems I: Regular Papers, **68**(4), pp. 1610-1623. https://doi.org/10.1109/TCSI.2021.3049268.

[30] Mamaghani, A. E., Khadem, S. E., and Bab, S., 2016, "Vibration Control of a Pipe Conveying Fluid under External Periodic Excitation Using a Nonlinear Energy Sink," Nonlinear Dyn., **86**(3), pp. 1761-1795. https://doi.org/10.1007/s11071-016-2992-x.

[31] Yang, T., Liu, T., Tang, Y., Hou, S., and Lv, X., 2019, "Enhanced Targeted Energy Transfer for Adaptive Vibration Suppression of Pipes Conveying Fluid," Nonlinear Dyn., **97**(3), pp. 1937-1944. https://doi.org/10.1007/s11071-018-4581-7.

[32] Chang, X., and Hong, X., 2024, "Stability and Nonlinear Vibration Characteristics of Cantilevered Fluid-Conveying Pipe with Nonlinear Energy Sink," Thin-Walled Structures, **205**. https://doi.org/10.1016/j.tws.2024.111987.

[33] Wang, Y., Li, X., and Shen, Y., 2024, "Study on Mechanical Vibration Control of Limit Cycle Oscillations in the Van Der Pol Oscillator by Means of Nonlinear Energy Sink," Journal of Vibration Engineering and Technologies, **12**(1), pp. 811-819. https://doi.org/10.1007/s42417-023-00877-w.

[34] Ma, K., Du, J., and Liu, Y., 2023, "A Study of Torsional Vibration Attenuation in Closed-Loop Crankshaft Model Using Absorbers with Cubic and Quintic Smooth Nonlinearities," Nonlinear Dyn., **111**(7), pp. 6017-6042. https://doi.org/10.1007/s11071-022-08165-0.

[35] Guo, H., Cao, S., Yang, T., and Chen, Y., 2018, "Aeroelastic Suppression of an Airfoil with Control Surface Using Nonlinear Energy Sink," Nonlinear Dyn., **94**(2), pp. 857-872. https://doi.org/10.1007/s11071-018-4398-4.

[36] Asme, M., Alighanbari, H., Paidoussis, M. P., and Asme, F., 1998, *C. Semler A Physical Explanation of the Destabilizing Effect of Damping*. [Online]. Available: http://asmedigitalcollection.asme.org/appliedmechanics/article-pdf/65/3/642/5466069/642_1.pdf.

[37] Ming, D., Shuai, M., Zhen, L., and Junhan, Z., 2024, "An Explanation for the Flutter Paradox in the Supercritical Region of a Simply-Supported Fluid-Conveying Pipe," Journal of Offshore Mechanics and Arctic Engineering, **146**(2). https://doi.org/10.1115/1.4062718.

[38] Dong, L., Chen, Z., Sun, M., and Sun, Q., 2023, "Phase Compensation Active Disturbance Rejection Control for Shimmy Vibration with Magnetorheological Damper of Aircraft," Expert Syst. Appl., **213**. https://doi.org/10.1016/j.eswa.2022.119126.

[39] Wang, Y., Jin, X., and Yin, Y., 2022, "Using Nonlinear Feedback Control to Improve Aircraft Nose Landing Gear Shimmy Performance," Meccanica, **57**(9), pp. 2395-2411. https://doi.org/10.1007/s11012-022-01560-2.

[40] Tartaruga, I., Cooper, J. E., Lowenberg, M. H., and Lemmens, Y., 2019, "Enhanced Evolutionary-Based Optimization Techniques Applied to a Nonlinear Landing Gear Design Problem," J. Aircr., **56**(5), pp. 2004-2018. https://doi.org/10.2514/1.C035198.

[41] Zhu, Y., Guo, X., and Cao, D., 2025, "Research Progress on Tuned Particle Dampers: A Review of Modeling, Energy Dissipation Mechanisms, and Applications," European Journal of Mechanics, A/Solids, **113**. https://doi.org/10.1016/j.euromechsol.2025.105720.

[42] Lei, X., Wu, C., and Chen, P., 2018, "Optimizing Parameter of Particle Damping Based on Leidenfrost Effect of Particle Flows," Mech. Syst. Signal Process., **104**, pp. 60-71. https://doi.org/10.1016/j.ymssp.2017.10.037.

[43] Doedel, E. J., Oldeman, B. E., Champneys, A. R., Dercole, F., Fairgrieve, T., Kuznetsov, Y., Paffenroth, R., Sandstede, B., Wang, X., and Zhang, C., 2012, *AUTO-07P : CONTINUATION AND BIFURCATION SOFTWARE FOR ORDINARY DIFFERENTIAL EQUATIONS*, Montreal, Canada.

[44] Dhooge, A., Govaerts, W., Kuznetsov, Yu. A., Meijer, H. G. E., and Sautois, B., 2008, "New Features of the Software MatCont for Bifurcation Analysis of Dynamical Systems," Math. Comput. Model. Dyn. Syst., **14**(2), pp. 147-175. https://doi.org/10.1080/13873950701742754.

Acknowledgment

This research is funded by the National Natural Science Foundation of China, grant numbers U25A20187, U2241264, and 12332001, Aeronautical Science Foundation (2023M072075002). Part of this work has been developed during the permanence of Dr. Tian Nan at the Polytechnic University of Marche, Ancona, Italy.